Mechanical properties of the rocky interiors of icy moons

Cassandra Seltzer[1], Hamed O Ghaffari[1], and Matěj Peč[2]

[1]Massachusetts Institute of Technology
[2]MIT EAPS

December 3, 2023

Abstract

Icy moons in the outer Solar System contain rocky, chondritic interiors, but this material is rarely studied under confining pressure. The contribution of rocky interiors to deformation and heat generation is therefore poorly constrained. We deformed LL6 chondrites at confining pressures [?] 100 MPa and quasistatic strain rates, and recorded acoustic emissions (AEs) using ultrasound probes. We defined a failure envelope, measured ultrasonic velocities, and retrieved elastic moduli for the experimental conditions. Chondritic material stiffened with increasing confining pressure, and reached its peak strength at 50 MPa confining pressure. Microcracking events occurred at low stresses, during nominally "elastic" deformation, indicating that dissipative processes are possible in rocky interiors. These events were most energetic at lower differential stresses, and occurred more frequently at lower confining pressures. We suggest that chondritic interiors of icy moons are therefore stronger, less compliant, and less dissipative with increasing pressure and size.

Mechanical Properties of the Rocky Interiors of Icy Moons

Cassandra Seltzer[1], Hoagy O. Ghaffari[1], Matěj Peč[1]

[1]Massachusetts Institute of Technology, Department of Earth, Atmospheric, and Planetary Sciences, Massachusetts, USA

Corresponding author: Cassandra Seltzer (cseltz@mit.edu)

Key points:

1. We established the failure envelope of chondritic materials under conditions relevant to the rocky interiors of small icy moons
2. Chondritic material has a yield cap around 50 MPa confining pressure, above which its porosity is very small
3. Pressurization and deformation of chondritic material creates energetic cracks, which could contribute to heat dissipation

Abstract

Icy moons in the outer Solar System contain rocky, chondritic interiors, but this material is rarely studied under confining pressure. The contribution of rocky interiors to deformation and heat generation is therefore poorly constrained. We deformed LL6 chondrites at confining pressures ≤ 100 MPa and quasistatic strain rates, and recorded acoustic emissions (AEs) using ultrasound probes. We defined a failure envelope, measured ultrasonic velocities, and retrieved elastic moduli for the experimental conditions. Chondritic material stiffened with increasing confining pressure, and reached its peak strength at 50 MPa confining pressure. Microcracking events occurred at low stresses, during nominally "elastic" deformation, indicating that dissipative processes are possible in rocky interiors. These events were most energetic at lower differential stresses, and occurred more frequently at lower confining pressures. We suggest that chondritic interiors of icy moons are therefore stronger, less compliant, and less dissipative with increasing pressure and size.

Plain language summary

Many icy moons in the outer Solar System have warm, active interiors, but the source of the heat that maintains this activity is sometimes unknown. Many of these moons contain rocky layers which are made of the same material as meteorites that have landed on the Earth. However, we have never previously studied how this material deforms under confining pressures like those found within icy moons. We conducted a lab study of the deformation mechanisms of meteoritic material to study how the deformation response applies to the interior of icy moons. We also analyzed cracking in response to small stress changes, which occurred at all stages of deformation. We found that the material behaved differently at low and high confining pressures, with a peak strength at ~50 MPa. This indicates that icy moons with smaller oceans and thinner crusts may deform differently than larger icy moons, and can receive some of the heat needed to maintain their oceans through cracking processes in their porous cores.

1. Introduction

Icy moons in the outer Solar System are considered excellent candidate bodies for hosting extraterrestrial life. The interior properties of these moons are important for determining the feasibility of life, lander missions, and future priorities in exploring the outer Solar System. The mechanical properties of the cores of these moons are relatively less well-studied than the properties of their icy crusts and water oceans, as the cores are likely less dissipative than the ice or liquid layers (e.g., Tobie et al., 2005). The deformation mechanisms of core material are thus presently still unknown, leaving large uncertainties as to how dissipation proceeds throughout the entire body: there is an order-of-magnitude difference in potential heat release from Enceladus' core, for example, depending on if it is stiff and elastic or if it is highly deformable and (poro)viscoelastic (Aygün and Čadek, 2022; Rovira-Navarro et al., 2022).

The yield strength of a material, which modelers use to predict how a body responds to stress, is almost always pressure-dependent, and often strain-rate dependent (Mair et al., 2002; Mulliken and Boyce, 2006). Rocky components of icy moons are frequently chondritic in nature (Kuskov and Kronrod, 2005; Néri et al., 2020; Neumann and Kruse, 2019), and most strength tests of meteoritic material are conducted at asteroidal conditions: no confinement, and fast strain rates.

Confining pressures at the core-ocean or core-mantle boundary of icy moons frequently reach tens of MPa and more (Neveu et al., 2015; Styczinski et al., 2022; Vance et al., 2018). Almost all tests on meteoritic material occur at room pressure (Pohl and Britt, 2020). The few tests that do assess strength and deformation mechanisms of chondritic material under pressure (Ramesh et al., 2017; Voropaev et al., 2017) do not report strength at pressures relevant to rocky interiors of icy moons. Voropaev et al. (2020) did study a single sample at confining pressure of 50 MPa, but did not apply any differential stress and therefore could not measure the strength of the material. Dynamic (fast) deformation experiments simulating crater formation and impacts on chondrites are also common. These experiments are not easily applied to planetary strain rates, and there is a larger rate sensitivity in unconfined meteoritic material than in terrestrial rocks (Kimberley and Ramesh, 2011). Hogan et al. (2015) used Brazilian disk tests in a Kolsky bar apparatus under confined planar configuration at dynamic strain rates of $10^1 - 10^3$ s^{-1}, which yielded a higher peak strength (~300 MPa) than the unconfined tests at similar strain rates, but did not record enough data at low strain rates to establish a definite change in peak strength for quasistatic tests conducted at no confining pressure vs. those conducted under confinement.

Here, we report the mechanical properties of deforming chondritic material under confining pressure. These measurements represent the first experimental investigation of chondritic material deformation under confining pressure similar to that found inside an icy moon. We used fallen meteoritic material, which is inherently pre-deformed and high-strength. These fallen meteorites are analogs for the rocky cores and mantles of moons, which have survived accretion and continuous tidal deformation for billions of years (Nimmo and Pappalardo, 2016).

In addition to the bulk mechanical response to deformation, we also studied microcracking behavior as the rocks were pressurized, and subsequently deformed at elevated confining pressures. Cracks associated with damage emit dynamic stress waves, observable as acoustic emissions (AEs) with characteristic frequencies depending on the source characteristics of deformation (Eitzen and Wadley, 1984; Ghaffari et al., 2014; Lei and Ma, 2014; Li et al., 2021; O'Ghaffari et al., 2023). The internal structure can also be sampled using throughgoing waves, which acquire signatures of the microstructure as they propagate through and interact with the material. We used ultrasonic probes in passive and active modes to measure 1) energy release associated with acoustic emissions, and 2) variations of sound velocities and their transmissivity in the samples under confining pressure. As macroscale behavior arises from microscale effects, data from all scales is needed to produce a robust picture of deformation dynamics.

This paper presents mechanical results from deformation tests, followed by observations of internal structure based on acoustic emissions and ultrasonic pulsing. We show that as the meteoritic material encounters higher confining pressures up to 50 MPa, the samples become stronger and emitted high-energy acoustic waves. Above 50 MPa confining pressure, the material became weaker, and dissipated less energy via AEs. Our observations indicate that the mechanisms of deformation are controlled by porosity closure, and that the dissipation of stored energy via microcracking is more pronounced at lower confining pressures.

2. Methods

These tests were conducted on samples from the Kilabo meteorite, an LL6 chondrite. Moons have broadly chondritic silicate interiors: Néri et al. (2020) suggest that the cores of Titan and Ganymede (and possibly Callisto) are carbonaceous chondrites, while Kuskov and Kronrod (2005) infer an low metallicity and/or low iron (L/LL) composition for the interior of Europa (and, again, possibly Callisto), and Neumann and Kruse (2019) find an ordinary chondritic (OC) composition (likely L/LL) for the rocky core of Enceladus. Previous experiments suggest that strength differences between carbonaceous and ordinary chondrites are related to the higher porosity of carbonaceous chondrites rather than any inherent difference in the material (Flynn et al., 2018; Pohl and Britt, 2020).

The meteoritic material was impregnated in epoxy before being drilled into 6.25 mm diameter cores for laboratory deformation. The samples were jacketed in soft PVC tubing, then encased in Teflon heat shrink tubing prior to deformation (Supplementary material). This material has ~15% microporosity and a mean density of ~2.5 g/cm^3. However, these (and other) properties are heterogeneously distributed throughout the sample. Samples were taken from the interior of the meteorite, and there is no alteration crust present. Deformation was performed in a Paterson gas medium deformation apparatus (Paterson, 1990) housed in the Rock Mechanics Laboratory at MIT. A summary of the experimental parameters can be found in Supplemental Table 1, and a setup schematic can be found in Figure S1.

We applied isostatic confining pressures (σ_3) of up to 100 MPa, and deformed the samples at room temperature (296 K) and constant strain rates of 10^{-5} s^{-1}, resulting in triaxial stress ($\sigma_1 > \sigma_3 = \sigma_2$). Differential stress ($|\sigma_1 - \sigma_3|$) continued to increase until failure, the point at which the samples no longer supported increasing stress and began to weaken (Figure 2a).

A custom data acquisition system (DAQ) was used in order to record passive AEs and pass active ultrasonic waves through the samples. Miniature piezoelectric sensors with a diameter of 1.5 mm were created by cementing a piezo-element (0.5 mm tall) within a metallic tube. The piezo-element was then coated with gold, to achieve high electrical conductivity. These sensors were attached to microsprings and threaded through pistons to allow constant coupling between the sensor and the sample during deformation. Signals were amplified at ~60 dB and recorded at 50 MS/s rate with 12 bit resolution using a digital oscilloscope (TiePie HS4-50). The majority of amplified signals fell in the frequency range of ~50 kHz to 2 MHz. One of the sensors was set to pulse P-waves (Y-cut LiNbO3), and the other one could receive both P and S waves (X-cut).

Microcracking occurred during both pressurization and deformation, releasing strain energy and causing vibrations within the sample. The received signals are recorded as displacements at the end of the sample, representing a convolution of three main controlling parameters of wave propagation: source characteristics, the medium through which waves travel, and the sensor response. We took Fourier Transforms of the displacements *u* at times *t* into corresponding frequencies ω, such that $u(\omega) = \sum_t u(t)e^{-i\omega t}$, with amplitudes $\psi_\alpha = \{u(\omega_\alpha)\}$ over frequency levels α. This expansion yields modulations to the energy state with amplitudes C_α and eigenvectors ϕ_α, which we use to characterize the state of the system $\vec{\psi}$ such that

$$\vec{\psi}(t) = \sum_\alpha C_\alpha e^{-i\omega_\alpha t}\vec{\phi}_\alpha.$$

For each acoustic emission, we smoothed over the raw emitted waveform with a window of 5 count intervals (0.1 μs), and denoised using wavelet decomposition. From this data, we computed a spectrogram using the window function W and time index τ to yield power P, such that

$$P(\tau, \omega) = \sum_t W(t-\tau)\psi(t)e^{-i\omega t} .$$

We integrated over the duration and frequency range of each event to compute the total power, then normalized by the mean power of background noise during each test. The power is a direct indication of how much energy was dissipated due to AEs. We present this quantity as a scalar value relative to the noise threshold, and discarded any events with a power-to-noise ratio below 1.5.

See Supplementary Information (figures S2, S3) for more details on acoustic emission data calibration and acquisition. A comprehensive proof of this integration can also be found in the discussion of the P-parameter by Ghaffari et al. (2021).

After deformation, entire samples were imaged with the table-top micro-computed tomography (micro-CT) Skyscan system at Woods Hole Oceanographic Institution, using 5-hour scan times at a 4 μm pixel size under 100 kV acceleration voltage.

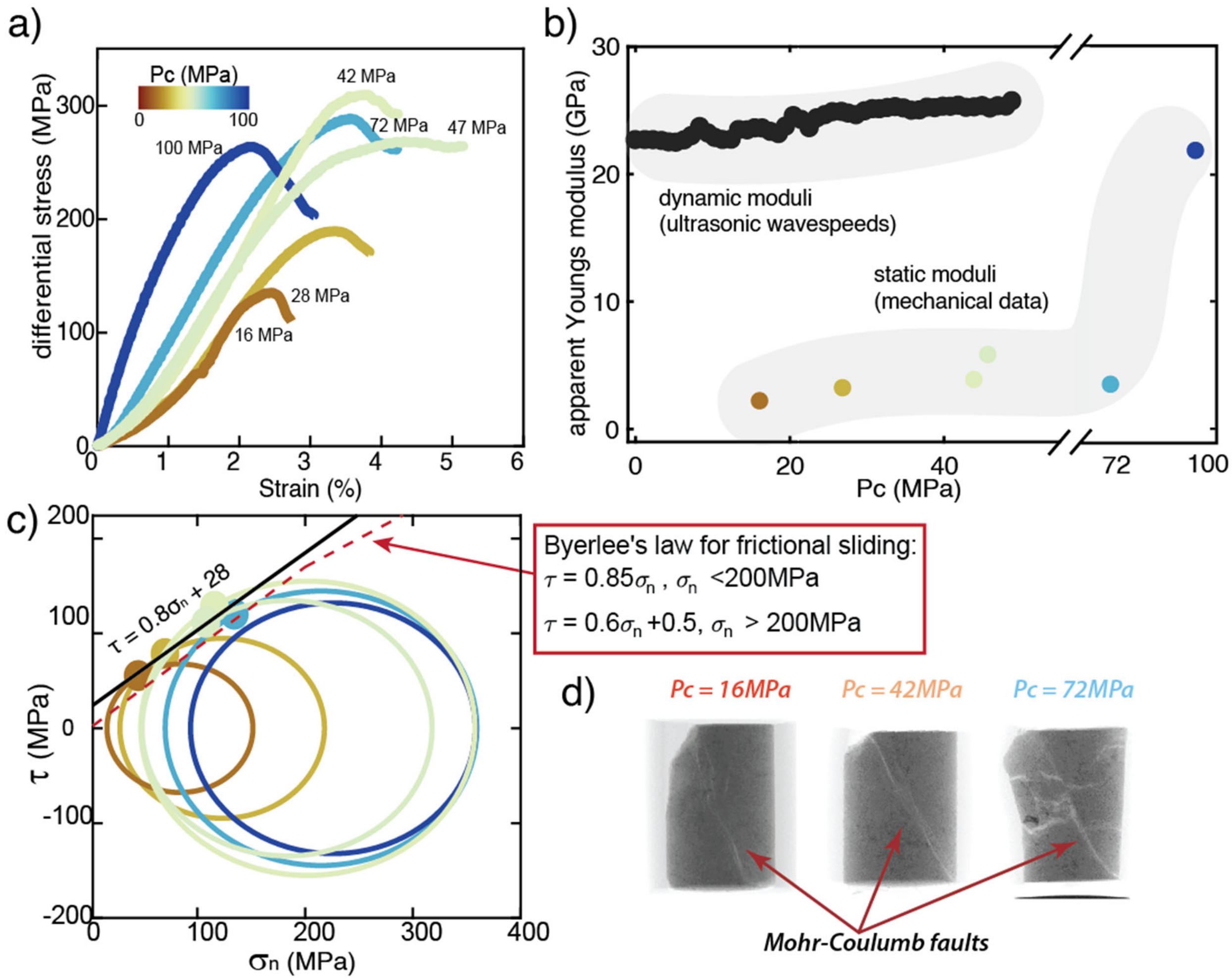

Figure 1: Mechanical results from deformation tests, represented as a) stress/strain curves, colored by confining pressure, b) observed Youngs moduli from ultrasonic and mechanical data, c) Mohr circles, with a tangent line indicating the Mohr-Coulomb failure envelope, large dots represent fault orientation developed at failure and d) CT images of deformed samples, with final faults from peak stress indicated.

3. Results

3.1. Mechanical data

The peak strength of the samples generally increased with confining pressure before reaching a maximum at ~50 MPa Pc (Figure 1a). Above ~50MPa confining pressure, peak strength decreased with increasing confining pressure. The σ_1 did not exceed ~350 MPa in any experiment, and so increases in confining pressure above 50 MPa lead to decreases in differential stress (Figure 1c). In all cases, the strain at peak strength at the point of failure remained close to 3%.

The failure envelopes of the experimentally deformed samples are represented as Mohr circles in Figure 2c. These Mohr circles are a graphical representation of the stress state within a rock at the point of failure, plotted in normal stress (σ_n) vs. shear stress (τ) space such that

$$\sigma_n = \frac{\sigma_1+\sigma_3}{2} + \frac{\sigma_1-\sigma_3}{2}\cos 2\theta \; ; \; \tau = \frac{\sigma_1-\sigma_3}{2}\sin 2\theta \, ,$$

where θ is the orientation of the normal to the fault plane with respect to σ_1. The Mohr-Coulomb failure envelope tangent to the circles indicates the stress conditions expected at failure:

$\tau = 0.8\sigma_n + 28$ (units in MPa).

This linear failure envelope is valid only for samples deformed below ~50 MPa Pc. Byerlee's Law, which defines the shear stress needed to slide rocks along a pre-existing fault surface, falls below the range of stress states recorded during deformation tests, as expected for the deformation of intact rocks. Notably, no test was able to reach σ_1 greater than 350 MPa; the three highest-pressure tests all failed at this point.

During several tests of up to 50 MPa confining pressure, we monitored sound velocities using the piezoelectric sensors placed above and below the sample (See Supplementary Table 1). From these measurements, we characterized dynamic (unrelaxed) Youngs moduli via p- and s-wave arrival times,

$$E_{dyn} = \frac{\rho V_S^2(3V_P^2-4V_S^2)}{V_P^2-V_S^2}.$$

We compared the unrelaxed, microscale E_{dyn} with the observed macroscale Youngs modulus derived from mechanical data on stress, σ, and strain, ε, such that

$$E_{qs} = \frac{\sigma}{\epsilon} \, .$$

As materials are stiffer at higher frequencies and shorter length scales (Jackson, 2015), the calculated Youngs modulus is higher during dynamic probing than during quasistatic bulk deformation (Figure 1b).

3.2. Ultrasonic probes

3.2.1. Acoustic emissions

All samples released energy via microcracking, both during pressurization and deformation. Microcracking occurred at all sampled pressures (Figure 2a, 2d). The integrated power and maximum amplitudes of each AEs decreased slightly with increasing differential stress ($|\sigma_1 - \sigma_3|$) (Figure 2b, 2e), and the power-to-noise ratio was largest for low values of σ_1 (Figure 2c, 2f). Many of these energetically dissipative events occurred during the nominally "elastic" deformation period, when differential stress is low and no energy release is expected. The material also emitted energy through microcracking during isotropic pressurization cycles (Figure 3d), when differential stress is zero.

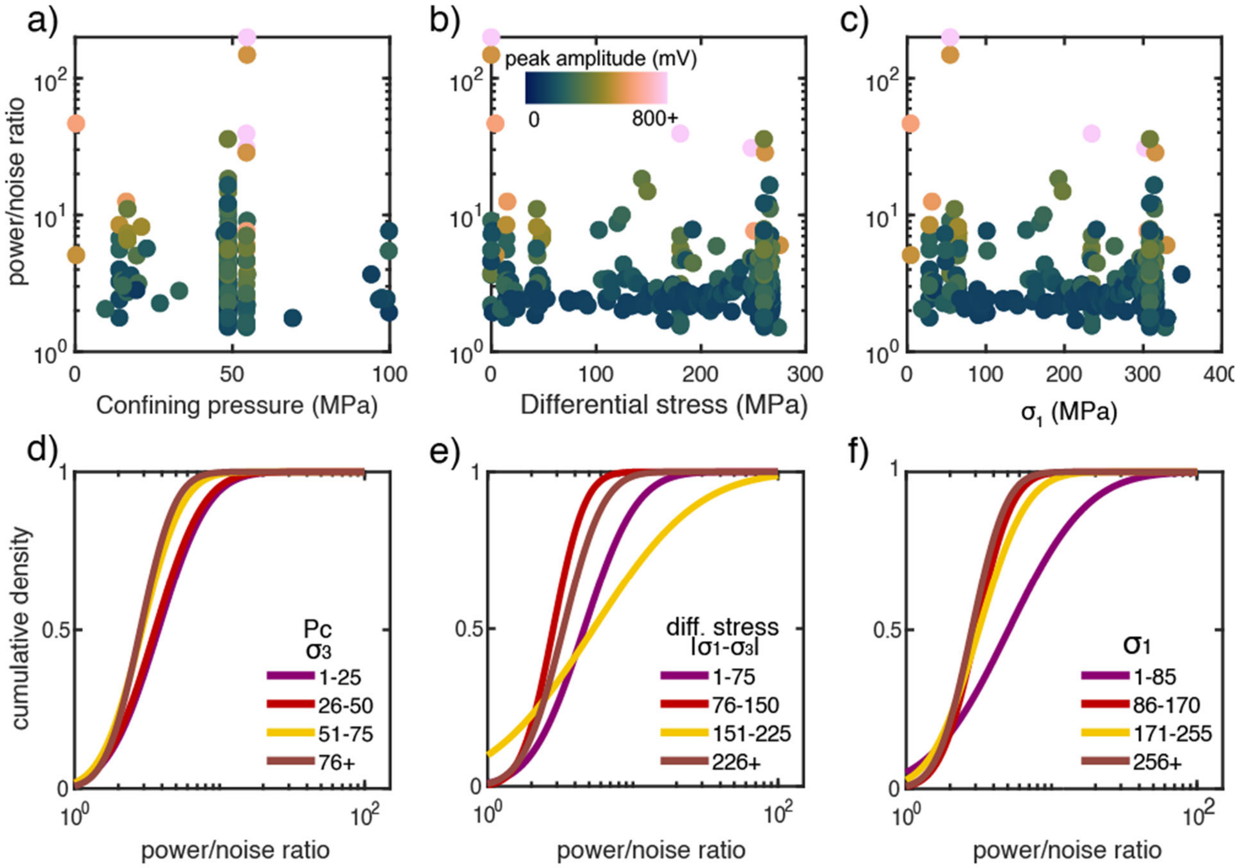

Figure 2: (a-c) Power of AEs, normalized by noise threshold for each test, as a function of a) confining pressure, b) differential stress, c) σ_1. Each point represents one AE event, and is colored by the maximum amplitude of that even following the colorbar in panel b). (d-f) Lognormal cumulative distribution functions of total power per event, evolving as a function of d) confining pressure, e) differential stress, and f) σ_1. Colored lines correspond to specific stress ranges, in MPa, which are defined specifically for each panel in its interior legend.

3.2.2. Ultrasonic pulsing

To determine wavespeeds as a function of pressure, we sent ultrasonic pulses through a sample while cycling confining pressure between 0 and 50 MPa, (Figure 3a, 3b, 3c). This procedure allowed us to examine if pressure oscillations changed the internal structure of our material and validate our results. We examined the entire waveform to see how the structure is affecting throughgoing waves (Figure 3d, 3e). The amplitudes and arrival times of throughgoing waves mimicked the pressure conditions, such that at lower pressures, comparable parts of the waveform arrived later, and at higher pressures, they arrived earlier (Figure 3d). The waveforms also remained similar at the same pressure even after a pressurization-depressurization cycle and associated AEs (Figure 3e; S5), suggesting that the modifications to internal structure of the material occur on smaller length scales than sampled by ultrasonic waves and therefore would not be visible to seismic waves, regardless of the pressure history.

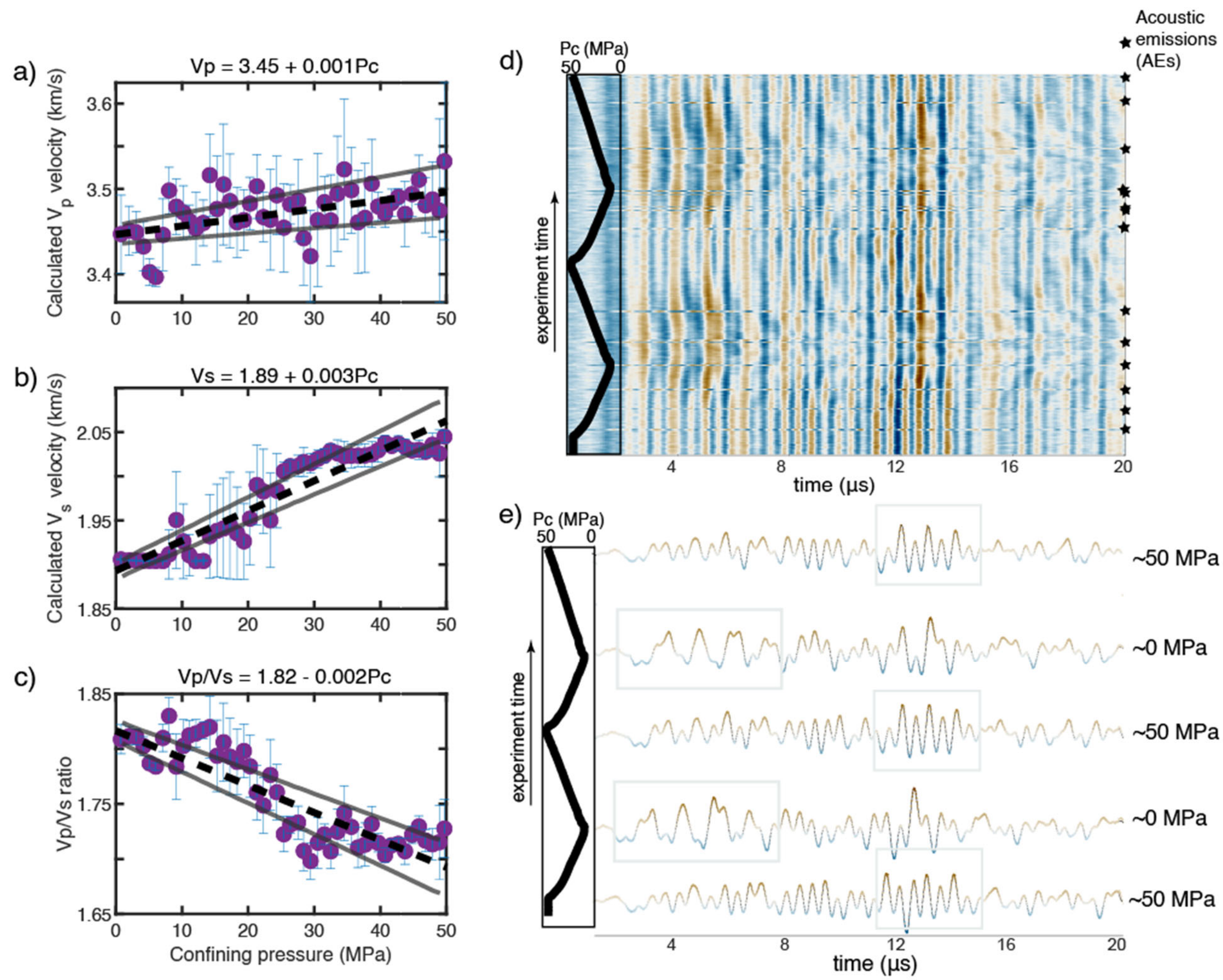

Figure 3: Results from ultrasonic pulsing during confining pressure oscillation. a) Vp wavespeeds. b) Vs wavespeeds. c) Vp/Vs ratio. For a-c, linear trendlines are shown in black, with grey lines denoting 90% confidence interval. d) Two full depressurization-repressurization cycles and resultant waveforms. Black line indicates pressure conditions. Waveforms are stacked with increasing experimental time, and color corresponds with amplitude over wavelength time, from blue (high negative amplitude) to brown (high positive amplitude). Horizontal, discontinuous lines marked with stars are energetic acoustic emission events, which are separate from the pulsed ultrasonic waves shown here. e) Sample waveforms from 0 and 50 MPa confining pressure at each inflection point in the cycle. Similar parts of the waveform at 0 and 50 MPa are highlighted in light grey boxes. See Supplementary Information for further discussion of waveform analysis (S4-6).

4. Discussion

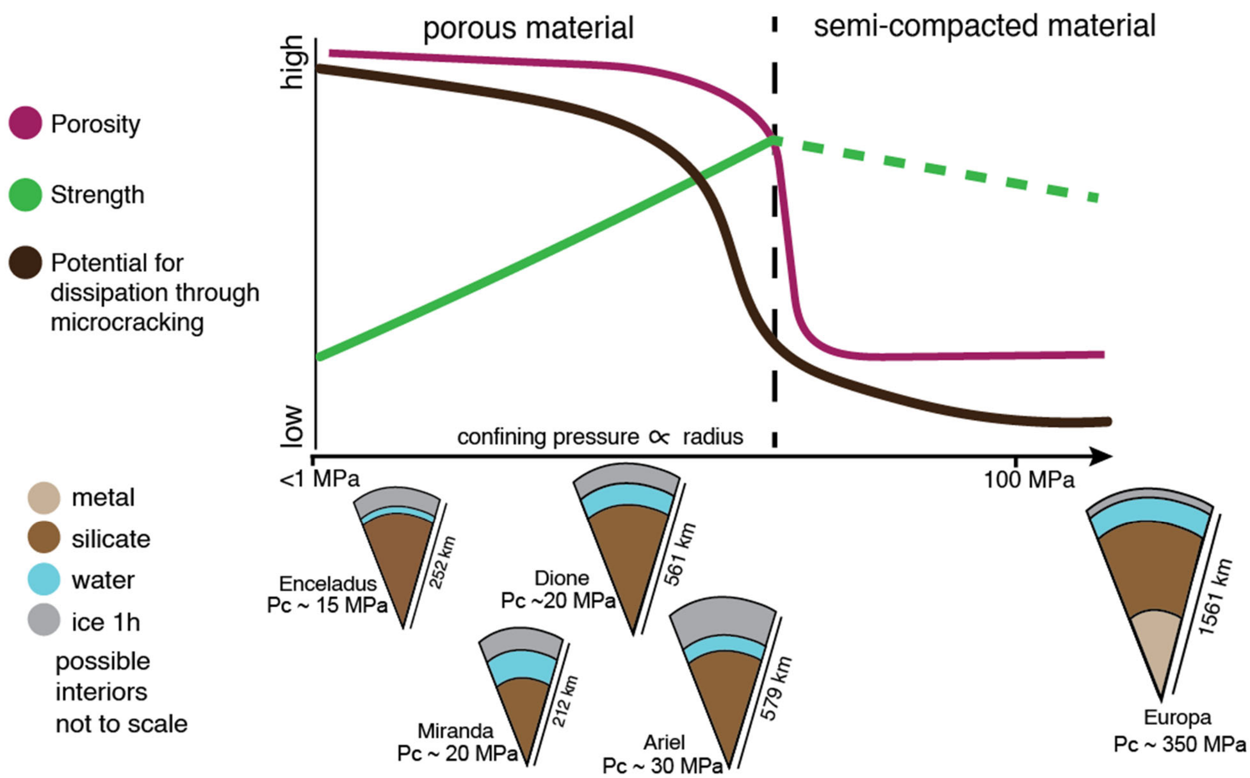

Figure 4: A conceptual diagram showing the effects of confining pressure on porosity, strength, and the power released via microcracking. Sample interior models for small icy moons are shown in order of increasing Pc at the ocean-rock interface, based on estimates from PlanetProfile by Vance et al (2018).

The above results show that the mechanical and acoustic properties of chondritic material, and therefore the cores of icy moons, are dependent on confining pressure. Several of these relationships are depicted schematically in Figure 4.

4.1. Discussion of mechanical data

Chondritic material initially strengthens with increasing confining pressure, then undergoes a drop in peak differential stress above confining pressures >50 MPa (Figure 1a, 1c). This behavior is similar to the "cap model" for compaction and deformation of porous Earth materials. In the cap model porosity drops steadily with increasing pressure before dropping rapidly at a point of compactive yield (C*), where the load-bearing framework collapses and above which cataclastic flow takes over as the primary mode of deformation (Wong and Baud, 2012).

Pore closure may therefore proceed in a predictable, yet discontinuous manner across icy moon environments. The maximum pressure at which porosity is maintained within a rocky interior should decrease with increasing Pc, then suddenly drop, rather than a slow closure similar to that within the outer layers of rocky planets as is often assumed in planetary models (e.g. Vance et al., 2018). The pores do not close entirely at this point, but most porosity is lost. It is possible that the maximum normal stress seen in our test, 350 MPa, represents the condition for total pore closure. Assumptions of density and permeability within cores should see a similar jump. These observations indicate that the mechanisms of deformation may be different in larger moons than in smaller moons, due to the increased confining pressures from increased overburden at the rock-ocean or rock-ice interface. In bodies where rocky interiors are under higher confining pressures, pore closure effects may not be as important and material may be stiffer; in lower-pressure environments, material may deform more easily.

Viscoelastic deformation of silicate interiors has been suggested as a mechanism for heat generation and tidal dissipation in Enceladus and Europa (Kang et al., 2020; Liao et al., 2020; Rovira-Navarro et al., 2022), but a true viscous response is unlikely in a cold, chondritic layer. Silicates typically require elevated pressures and temperatures for viscous deformation (e.g. Kohlstedt and Hansen, 2015). Brittle creep, a mechanism that is active in silicate rocks at low pressures and temperatures (Bernabé and Peč, 2022; Brantut et al., 2013) may generate an additional apparent viscous response, contributing to the total heat dissipation via microcracking. Similar effects may arise from pore closure and reopening. While not truly a viscous response, the presence of brittle creep could serve as a nonlinear viscous element over short timescales and thus should be considered in models for viscoelastic core deformation.

4.2. Discussion of acoustic and ultrasonic data

Dissipative acoustic emissions from microcracking events occurred at all pressures sampled, even at low differential stresses, indicating that even small changes to local stresses can initiate cracks (Figure 2). The Vp/Vs ratio also decreased with increasing confining pressure (Figure 3c), which occurs as damage increases (Wang et al., 2012). We suggest that microcracking could be continuously occurring in rocky interiors of icy satellites, where deviatoric stresses can be on the order of 1 MPa or higher, changing periodically with the orbit of the satellite (Gao and Stevenson, 2013; McKinnon, 2013). As these cracks occurred during the nominally elastic component of deformation (low differential stress, low strain; see Figure 2b, 2e), we suggest that that the energy from these microscale plastic mechanisms should be associated with the apparent viscous response necessary for dissipation in the silicate core.

Moons with thinner crusts and oceans could receive proportionally more heat over their lifetimes from the deformation of their rocky interiors than larger moons, as their cores will be more deformable at low pressures and therefore able to dissipate heat during viscoelastic deformation. Local values of σ_1 will be lower in smaller moons as well, corresponding to the most energetic cracking events seen in our tests (Figure 2c, 2f). As this energy is released, it could contribute to processes such as ice overturn, ocean maintenance, and possibly even geyser activity as seen on Enceladus' south pole. Pore fluids change the local stress state by lowering the effective pressure, so that materials at the ocean-silicate interface could experience even more fracture than we observe in lab. Additionally, while our deformation experiments are conducted at relatively slow strain rates, they are not identical to timescales and frequencies of tidal deformation. Under realistic tidal forcing periods, the strength of porous rocks is lower (Bagde and Petroš, 2009; Peng et al., 2020), increasing the likelihood of cracking in response to small stress changes. One excellent opportunity for future laboratory studies is the measurement of acoustic properties of aqueously altered chondritic material, which should exist at the rock-ocean boundary.

In addition to releasing heat at the time of their formation, cracks create new surface area. Modeling by Rovira-Navarro et al. (2022) found that rock-water interaction (via increasing permeability) increases dissipation throughout a porous core. Fresh surface area would encourage serpentinization, which has been suggested as a mechanism for generating hydrogen within the oceans of icy bodies (Kamata et al., 2019; McCollom et al., 2022; Neveu et al., 2015; Vance and Melwani Daswani, 2020) or cultivation of organic materials which have risen to Titan's surface (Castillo-Rogez and Lunine, 2010). Many of these reactions include volume increase which modifies the local stress field, encouraging further cracking within the silicate body and providing a self-sustaining heating process.

5. Conclusions

We characterized the mechanical properties of stony chondritic material under a range of confining pressures, defined a failure envelope, measured wavespeeds, and retrieved both static and dynamic elastic moduli. The mechanical results suggest that porosity decreases significantly at lab confining pressure of ~50 MPa, such that the silicate interiors of larger icy moons will be relatively dense and impermeable. The interiors of larger moons are less deformable, and therefore contribute proportionally less energy in response to tidal forcing, than those of smaller moons. We also observed semi-continuous energy release arising from microcracking under small changes to stress. These microcracks may represent an apparent viscous response which enhances heat dissipation within rocky cores and mantles. The energy release from microcracking occurred during pressurization and depressurization as well, and transmissivity of the material (likely dependent on its porosity) was a function of current confining pressure rather than pressure history. Pressure, and the resultant amount of porosity that a material can maintain, is therefore a strong control on the dissipative potential of silicate interiors. These findings are useful for determining the level of heat generated in the cores and mantles of icy moons, which may then drive ocean circulation and/or maintenance. We also see that the release of energy persists as deformation continues, indicating that ongoing deformation on a diurnal timescale may remain important for the total heat flux of an icy body.

Acknowledgements: CS received support from Massachusetts Space Grant fellowship and MathWorks. Figures were plotted using perceptually uniform colormaps from Crameri (2021). CORD laboratory technician support by NSF grant # 2054414 is gratefully acknowledged. Thank you to Veronique LeRoux for CT scans, Mark Panning, Mohit Melwani Deswani, and Laurent Pou for discussions on icy moon interiors, and to Rick Binzel for early input on the project.

Data Availability Statement: All mechanical, ultrasonic, and acoustic data can be found at https://zenodo.org/records/10211457 (Seltzer, 2023).

Aygün, B., Čadek, O., 2022. A new approach to modeling the tidal dissipation in subsurface oceans of icy moons of Jupiter and Saturn (other). oral. https://doi.org/10.5194/epsc2022-968

Bagde, M.N., Petroš, V., 2009. Fatigue and dynamic energy behaviour of rock subjected to cyclical loading. International Journal of Rock Mechanics and Mining Sciences 46, 200–209. https://doi.org/10.1016/j.ijrmms.2008.05.002

Bernabé, Y., Peč, M., 2022. Brittle Creep and Failure: A Reformulation of the Wing Crack Model. Journal of Geophysical Research: Solid Earth 127, e2022JB024610. https://doi.org/10.1029/2022JB024610
Brantut, N., Heap, M.J., Meredith, P.G., Baud, P., 2013. Time-dependent cracking and brittle creep in crustal rocks: A review. Journal of Structural Geology 52, 17–43. https://doi.org/10.1016/j.jsg.2013.03.007
Castillo-Rogez, J.C., Lunine, J.I., 2010. Evolution of Titan's rocky core constrained by Cassini observations. Geophysical Research Letters 37. https://doi.org/10.1029/2010GL044398
Crameri, F., 2021. Scientific colour maps. https://doi.org/10.5281/zenodo.5501399
Eitzen, D.G., Wadley, H.N.G., 1984. Acoustic Emission: Establishing the Fundamentals. J. RES. NATL. BUR. STAN. 89, 75. https://doi.org/10.6028/jres.089.008
Flynn, G.J., Consolmagno, G.J., Brown, P., Macke, R.J., 2018. Physical properties of the stone meteorites: Implications for the properties of their parent bodies. Geochemistry 78, 269–298. https://doi.org/10.1016/j.chemer.2017.04.002
Gao, P., Stevenson, D.J., 2013. Nonhydrostatic effects and the determination of icy satellites' moment of inertia. Icarus 226, 1185–1191. https://doi.org/10.1016/j.icarus.2013.07.034
Ghaffari, H.O., Mok, U., Pec, M., 2021. On calibration of piezoelectric sensors with laser doppler vibrometer. The Journal of the Acoustical Society of America 150, 2503–2513. https://doi.org/10.1121/10.0006445
Ghaffari, H.O., Nasseri, M.H.B., Young, R.P., 2014. Faulting of Rocks in a Three-Dimensional Stress Field by Micro-Anticracks. Sci Rep 4, 5011. https://doi.org/10.1038/srep05011
Hogan, J.D., Kimberley, J., Hazeli, K., Plescia, J., Ramesh, K.T., 2015. Dynamic behavior of an ordinary chondrite: The effects of microstructure on strength, failure and fragmentation. Icarus 260, 308–319. https://doi.org/10.1016/j.icarus.2015.07.027
Jackson, I., 2015. Properties of Rocks and Minerals: Physical Origins of Anelasticity and Attenuation in Rock, in: Treatise on Geophysics. Elsevier, pp. 539–571. https://doi.org/10.1016/B978-0-444-53802-4.00045-2
Kamata, S., Nimmo, F., Sekine, Y., Kuramoto, K., Noguchi, N., Kimura, J., Tani, A., 2019. Pluto's ocean is capped and insulated by gas hydrates. Nat. Geosci. 12, 407–410. https://doi.org/10.1038/s41561-019-0369-8
Kang, W., Bire, S., Campin, J.-M., Sotin, C., German, C., Thurnherr, A., Marshall, J., 2020. Differing Enceladean ocean circulation and ice shell geometries driven by tidal heating in the ice versus the core.
Kimberley, J., Ramesh, K.T., 2011. The dynamic strength of an ordinary chondrite. Meteoritics & Planetary Science 46, 1653–1669. https://doi.org/10.1111/j.1945-5100.2011.01254.x
Kohlstedt, D.L., Hansen, L.N., 2015. Constitutive Equations, Rheological Behavior, and Viscosity of Rocks, in: Treatise on Geophysics. Elsevier, pp. 441–472. https://doi.org/10.1016/B978-0-444-53802-4.00042-7
Kuskov, O.L., Kronrod, V.A., 2005. Internal structure of Europa and Callisto. Icarus, Europa Icy Shell 177, 550–569. https://doi.org/10.1016/j.icarus.2005.04.014
Lei, X., Ma, S., 2014. Laboratory acoustic emission study for earthquake generation process. Earthq Sci 27, 627–646. https://doi.org/10.1007/s11589-014-0103-y
Li, X., Si, G., Oh, J., Canbulat, I., Xiang, Z., Zhang, X., 2021. Laboratory characterisation of anisotropic and heterogeneous damage of rock sample using acoustic emission and ultrasonic monitoring technologies. IOP Conf. Ser.: Earth Environ. Sci. 861, 022040. https://doi.org/10.1088/1755-1315/861/2/022040
Liao, Y., Nimmo, F., Neufeld, J.A., 2020. Heat Production and Tidally Driven Fluid Flow in the Permeable Core of Enceladus. Journal of Geophysical Research: Planets 125, e2019JE006209. https://doi.org/10.1029/2019JE006209

Mair, K., Elphick, S., Main, I., 2002. Influence of confining pressure on the mechanical and structural evolution of laboratory deformation bands. Geophysical Research Letters 29, 49-1-49–4. https://doi.org/10.1029/2001GL013964
McCollom, T.M., Klein, F., Ramba, M., 2022. Hydrogen generation from serpentinization of iron-rich olivine on Mars, icy moons, and other planetary bodies. Icarus 372, 114754. https://doi.org/10.1016/j.icarus.2021.114754
McKinnon, W.B., 2013. The shape of Enceladus as explained by an irregular core: Implications for gravity, libration, and survival of its subsurface ocean. Journal of Geophysical Research: Planets 118, 1775–1788. https://doi.org/10.1002/jgre.20122
Mulliken, A.D., Boyce, M.C., 2006. Mechanics of the rate-dependent elastic–plastic deformation of glassy polymers from low to high strain rates. International Journal of Solids and Structures 43, 1331–1356. https://doi.org/10.1016/j.ijsolstr.2005.04.016
Néri, A., Guyot, F., Reynard, B., Sotin, C., 2020. A carbonaceous chondrite and cometary origin for icy moons of Jupiter and Saturn. Earth and Planetary Science Letters 530, 115920. https://doi.org/10.1016/j.epsl.2019.115920
Neumann, W., Kruse, A., 2019. Differentiation of Enceladus and Retention of a Porous Core. ApJ 882, 47. https://doi.org/10.3847/1538-4357/ab2fcf
Neveu, M., Desch, S.J., Castillo-Rogez, J.C., 2015. Core cracking and hydrothermal circulation can profoundly affect Ceres' geophysical evolution. Journal of Geophysical Research: Planets 120, 123–154. https://doi.org/10.1002/2014JE004714
Nimmo, F., Pappalardo, R.T., 2016. Ocean worlds in the outer solar system. Journal of Geophysical Research: Planets 121, 1378–1399. https://doi.org/10.1002/2016JE005081
O'Ghaffari, H., Peč, M., Mittal, T., Mok, U., Chang, H., Evans, B., 2023. Microscopic defect dynamics during a brittle-to-ductile transition. Proceedings of the National Academy of Sciences 120, e2305667120. https://doi.org/10.1073/pnas.2305667120
Paterson, M.S., 1990. Rock Deformation Experimentation, in: The Brittle-Ductile Transition in Rocks. American Geophysical Union (AGU), pp. 187–194. https://doi.org/10.1029/GM056p0187
Peng, K., Zhou, J., Zou, Q., Song, X., 2020. Effect of loading frequency on the deformation behaviours of sandstones subjected to cyclic loads and its underlying mechanism. International Journal of Fatigue 131, 105349. https://doi.org/10.1016/j.ijfatigue.2019.105349
Pohl, L., Britt, D.T., 2020. Strengths of meteorites—An overview and analysis of available data. Meteoritics & Planetary Science 55, 962–987. https://doi.org/10.1111/maps.13449
Ramesh, K.T., Stickle, A.M., Kimberley, J., 2017. Rocks, Shocks and Asteroids, and Some Interesting Research Directions in Mechanics: 2015 Murray Lecture Paper. Experimental Mechanics 57, 1149–1159. https://doi.org/10.1007/s11340-017-0324-9
Rovira-Navarro, M., Katz, R.F., Liao, Y., van der Wal, W., Nimmo, F., 2022. The Tides of Enceladus' Porous Core. Journal of Geophysical Research: Planets 127, e2021JE007117. https://doi.org/10.1029/2021JE007117
Seltzer, C., 2023. Supporting data for "Mechanical properties of the rocky interiors of icy moons" [DATASET]. https://doi.org/10.5281/zenodo.10211457
Styczinski, M.J., Vance, S.D., Melwani Daswani, M., 2022. PlanetProfile: Self-consistent interior structure modeling for terrestrial bodies in Python (preprint). Planetology. https://doi.org/10.1002/essoar.10512890.1
Tobie, G., Mocquet, A., Sotin, C., 2005. Tidal dissipation within large icy satellites: Applications to Europa and Titan. Icarus, Europa Icy Shell 177, 534–549. https://doi.org/10.1016/j.icarus.2005.04.006
Vance, S.D., Melwani Daswani, M., 2020. Serpentinite and the search for life beyond Earth. Philosophical Transactions of the Royal Society A: Mathematical, Physical and Engineering Sciences 378, 20180421. https://doi.org/10.1098/rsta.2018.0421
Vance, S.D., Panning, M.P., Stähler, S., Cammarano, F., Bills, B.G., Tobie, G., Kamata, S., Kedar, S., Sotin, C., Pike, W.T., Lorenz, R., Huang, H.-H., Jackson, J.M., Banerdt, B., 2018. Geophysical

Investigations of Habitability in Ice-Covered Ocean Worlds. Journal of Geophysical Research: Planets 123, 180–205. https://doi.org/10.1002/2017JE005341

Voropaev, S.A., Kocherov, A.V., Lorenz, C.A., Korochantsev, A.V., Dushenko, N.V., Kuzina, D.M., Nugmanov, I.I., Jianguo, Y., 2017. Features in constructing a certificate of strength of extraterrestrial material by the example of the Chelyabinsk meteorite. Dokl. Phys. 62, 486–489. https://doi.org/10.1134/S1028335817100111

Voropaev, S.A., Nugmanov, I.I., Dushenko, N.V., Jianguo, Y., 2020. Dependence of the Elastic Properties of H5-Chondrites (NWA 12370) on Pressure. Dokl. Phys. 65, 383–386. https://doi.org/10.1134/S1028335820110105

Wang, X.-Q., Schubnel, A., Fortin, J., David, E.C., Guéguen, Y., Ge, H.-K., 2012. High Vp/Vs ratio: Saturated cracks or anisotropy effects? Geophysical Research Letters 39. https://doi.org/10.1029/2012GL051742

Mechanical Properties of the Rocky Interiors of Icy Moons

Cassandra Seltzer[1], Hoagy O. Ghaffari[1], Matěj Peč[1]

[1]Massachusetts Institute of Technology, Department of Earth, Atmospheric, and Planetary Sciences, Massachusetts, USA

Corresponding author: Cassandra Seltzer (cseltz@mit.edu)

Key points:

1. We established the failure envelope of chondritic materials under conditions relevant to the rocky interiors of small icy moons
2. Chondritic material has a yield cap around 50 MPa confining pressure, above which its porosity is very small
3. Pressurization and deformation of chondritic material creates energetic cracks, which could contribute to heat dissipation

Abstract

Icy moons in the outer Solar System contain rocky, chondritic interiors, but this material is rarely studied under confining pressure. The contribution of rocky interiors to deformation and heat generation is therefore poorly constrained. We deformed LL6 chondrites at confining pressures ≤ 100 MPa and quasistatic strain rates, and recorded acoustic emissions (AEs) using ultrasound probes. We defined a failure envelope, measured ultrasonic velocities, and retrieved elastic moduli for the experimental conditions. Chondritic material stiffened with increasing confining pressure, and reached its peak strength at 50 MPa confining pressure. Microcracking events occurred at low stresses, during nominally "elastic" deformation, indicating that dissipative processes are possible in rocky interiors. These events were most energetic at lower differential stresses, and occurred more frequently at lower confining pressures. We suggest that chondritic interiors of icy moons are therefore stronger, less compliant, and less dissipative with increasing pressure and size.

Plain language summary

Many icy moons in the outer Solar System have warm, active interiors, but the source of the heat that maintains this activity is sometimes unknown. Many of these moons contain rocky layers which are made of the same material as meteorites that have landed on the Earth. However, we have never previously studied how this material deforms under confining pressures like those found within icy moons. We conducted a lab study of the deformation mechanisms of meteoritic material to study how the deformation response applies to the interior of icy moons. We also analyzed cracking in response to small stress changes, which occurred at all stages of deformation. We found that the material behaved differently at low and high confining pressures, with a peak strength at ~50 MPa. This indicates that icy moons with smaller oceans and thinner crusts may deform differently than larger icy moons, and can receive some of the heat needed to maintain their oceans through cracking processes in their porous cores.

1. Introduction

Icy moons in the outer Solar System are considered excellent candidate bodies for hosting extraterrestrial life. The interior properties of these moons are important for determining the feasibility of life, lander missions, and future priorities in exploring the outer Solar System. The mechanical properties of the cores of these moons are relatively less well-studied than the properties of their icy crusts and water oceans, as the cores are likely less dissipative than the ice or liquid layers (e.g., Tobie et al., 2005). The deformation mechanisms of core material are thus presently still unknown, leaving large uncertainties as to how dissipation proceeds throughout the entire body: there is an order-of-magnitude difference in potential heat release from Enceladus' core, for example, depending on if it is stiff and elastic or if it is highly deformable and (poro)viscoelastic (Aygün and Čadek, 2022; Rovira-Navarro et al., 2022).

The yield strength of a material, which modelers use to predict how a body responds to stress, is almost always pressure-dependent, and often strain-rate dependent (Mair et al., 2002; Mulliken and Boyce, 2006). Rocky components of icy moons are frequently chondritic in nature (Kuskov and Kronrod, 2005; Néri et al., 2020; Neumann and Kruse, 2019), and most strength tests of meteoritic material are conducted at asteroidal conditions: no confinement, and fast strain rates.

Confining pressures at the core-ocean or core-mantle boundary of icy moons frequently reach tens of MPa and more (Neveu et al., 2015; Styczinski et al., 2022; Vance et al., 2018). Almost all tests on meteoritic material occur at room pressure (Pohl and Britt, 2020). The few tests that do assess strength and deformation mechanisms of chondritic material under pressure (Ramesh et al., 2017; Voropaev et al., 2017) do not report strength at pressures relevant to rocky interiors of icy moons. Voropaev et al. (2020) did study a single sample at confining pressure of 50 MPa, but did not apply any differential stress and therefore could not measure the strength of the material. Dynamic (fast) deformation experiments simulating crater formation and impacts on chondrites are also common. These experiments are not easily applied to planetary strain rates, and there is a larger rate sensitivity in unconfined meteoritic material than in terrestrial rocks (Kimberley and Ramesh, 2011). Hogan et al. (2015) used Brazilian disk tests in a Kolsky bar apparatus under confined planar configuration at dynamic strain rates of $10^1 – 10^3$ s^{-1}, which yielded a higher peak strength (~300 MPa) than the unconfined tests at similar strain rates, but did not record enough data at low strain rates to establish a definite change in peak strength for quasistatic tests conducted at no confining pressure vs. those conducted under confinement.

Here, we report the mechanical properties of deforming chondritic material under confining pressure. These measurements represent the first experimental investigation of chondritic material deformation under confining pressure similar to that found inside an icy moon. We used fallen meteoritic material, which is inherently pre-deformed and high-strength. These fallen meteorites are analogs for the rocky cores and mantles of moons, which have survived accretion and continuous tidal deformation for billions of years (Nimmo and Pappalardo, 2016).

In addition to the bulk mechanical response to deformation, we also studied microcracking behavior as the rocks were pressurized, and subsequently deformed at elevated confining pressures. Cracks associated with damage emit dynamic stress waves, observable as acoustic emissions (AEs) with characteristic frequencies depending on the source characteristics of deformation (Eitzen and Wadley, 1984; Ghaffari et al., 2014; Lei and Ma, 2014; Li et al., 2021; O'Ghaffari et al., 2023). The internal structure can also be sampled using throughgoing waves, which acquire signatures of the microstructure as they propagate through and interact with the material. We used ultrasonic probes in passive and active modes to measure 1) energy release associated with acoustic emissions, and 2) variations of sound velocities and their transmissivity in the samples under confining pressure. As macroscale behavior arises from microscale effects, data from all scales is needed to produce a robust picture of deformation dynamics.

This paper presents mechanical results from deformation tests, followed by observations of internal structure based on acoustic emissions and ultrasonic pulsing. We show that as the meteoritic material encounters higher confining pressures up to 50 MPa, the samples become stronger and emitted high-energy acoustic waves. Above 50 MPa confining pressure, the material became weaker, and dissipated less energy via AEs. Our observations indicate that the mechanisms of deformation are controlled by porosity closure, and that the dissipation of stored energy via microcracking is more pronounced at lower confining pressures.

2. Methods

These tests were conducted on samples from the Kilabo meteorite, an LL6 chondrite. Moons have broadly chondritic silicate interiors: Néri et al. (2020) suggest that the cores of Titan and Ganymede (and possibly Callisto) are carbonaceous chondrites, while Kuskov and Kronrod (2005) infer an low metallicity and/or low iron (L/LL) composition for the interior of Europa (and, again, possibly Callisto), and Neumann and Kruse (2019) find an ordinary chondritic (OC) composition (likely L/LL) for the rocky core of Enceladus. Previous experiments suggest that strength differences between carbonaceous and ordinary chondrites are related to the higher porosity of carbonaceous chondrites rather than any inherent difference in the material (Flynn et al., 2018; Pohl and Britt, 2020).

The meteoritic material was impregnated in epoxy before being drilled into 6.25 mm diameter cores for laboratory deformation. The samples were jacketed in soft PVC tubing, then encased in Teflon heat shrink tubing prior to deformation (Supplementary material). This material has ~15% microporosity and a mean density of ~2.5 g/cm^3. However, these (and other) properties are heterogeneously distributed throughout the sample. Samples were taken from the interior of the meteorite, and there is no alteration crust present. Deformation was performed in a Paterson gas medium deformation apparatus (Paterson, 1990) housed in the Rock Mechanics Laboratory at MIT. A summary of the experimental parameters can be found in Supplemental Table 1, and a setup schematic can be found in Figure S1.

We applied isostatic confining pressures (σ_3) of up to 100 MPa, and deformed the samples at room temperature (296 K) and constant strain rates of 10^{-5} s^{-1}, resulting in triaxial stress ($\sigma_1 > \sigma_3 = \sigma_2$). Differential stress ($|\sigma_1 - \sigma_3|$) continued to increase until failure, the point at which the samples no longer supported increasing stress and began to weaken (Figure 2a).

A custom data acquisition system (DAQ) was used in order to record passive AEs and pass active ultrasonic waves through the samples. Miniature piezoelectric sensors with a diameter of 1.5 mm were created by cementing a piezo-element (0.5 mm tall) within a metallic tube. The piezo-element was then coated with gold, to achieve high electrical conductivity. These sensors were attached to microsprings and threaded through pistons to allow constant coupling between the sensor and the sample during deformation. Signals were amplified at ~60 dB and recorded at 50 MS/s rate with 12 bit resolution using a digital oscilloscope (TiePie HS4-50). The majority of amplified signals fell in the frequency range of ~50 kHz to 2 MHz. One of the sensors was set to pulse P-waves (Y-cut $LiNbO_3$), and the other one could receive both P and S waves (X-cut).

Microcracking occurred during both pressurization and deformation, releasing strain energy and causing vibrations within the sample. The received signals are recorded as displacements at the end of the sample, representing a convolution of three main controlling parameters of wave propagation: source characteristics, the medium through which waves travel, and the sensor response. We took Fourier Transforms of the displacements u at times t into corresponding frequencies ω, such that $u(\omega) = \sum_t u(t)e^{-i\omega t}$, with amplitudes $\psi_\alpha = \{u(\omega_\alpha)\}$ over frequency levels α. This expansion yields modulations to the energy state with amplitudes C_α and eigenvectors ϕ_α, which we use to characterize the state of the system $\vec{\psi}$ such that

$$\vec{\psi}(t) = \sum_\alpha C_\alpha e^{-i\omega_\alpha t}\vec{\phi}_\alpha.$$

For each acoustic emission, we smoothed over the raw emitted waveform with a window of 5 count intervals (0.1 μs), and denoised using wavelet decomposition. From this data, we computed a spectrogram using the window function W and time index τ to yield power P, such that

$$P(\tau,\omega) = \sum_t W(t-\tau)\psi(t)e^{-i\omega t} .$$

We integrated over the duration and frequency range of each event to compute the total power, then normalized by the mean power of background noise during each test. The power is a direct indication of how much energy was dissipated due to AEs. We present this quantity as a scalar value relative to the noise threshold, and discarded any events with a power-to-noise ratio below 1.5.

See Supplementary Information (figures S2, S3) for more details on acoustic emission data calibration and acquisition. A comprehensive proof of this integration can also be found in the discussion of the P-parameter by Ghaffari et al. (2021).

After deformation, entire samples were imaged with the table-top micro-computed tomography (micro-CT) Skyscan system at Woods Hole Oceanographic Institution, using 5-hour scan times at a 4 μm pixel size under 100 kV acceleration voltage.

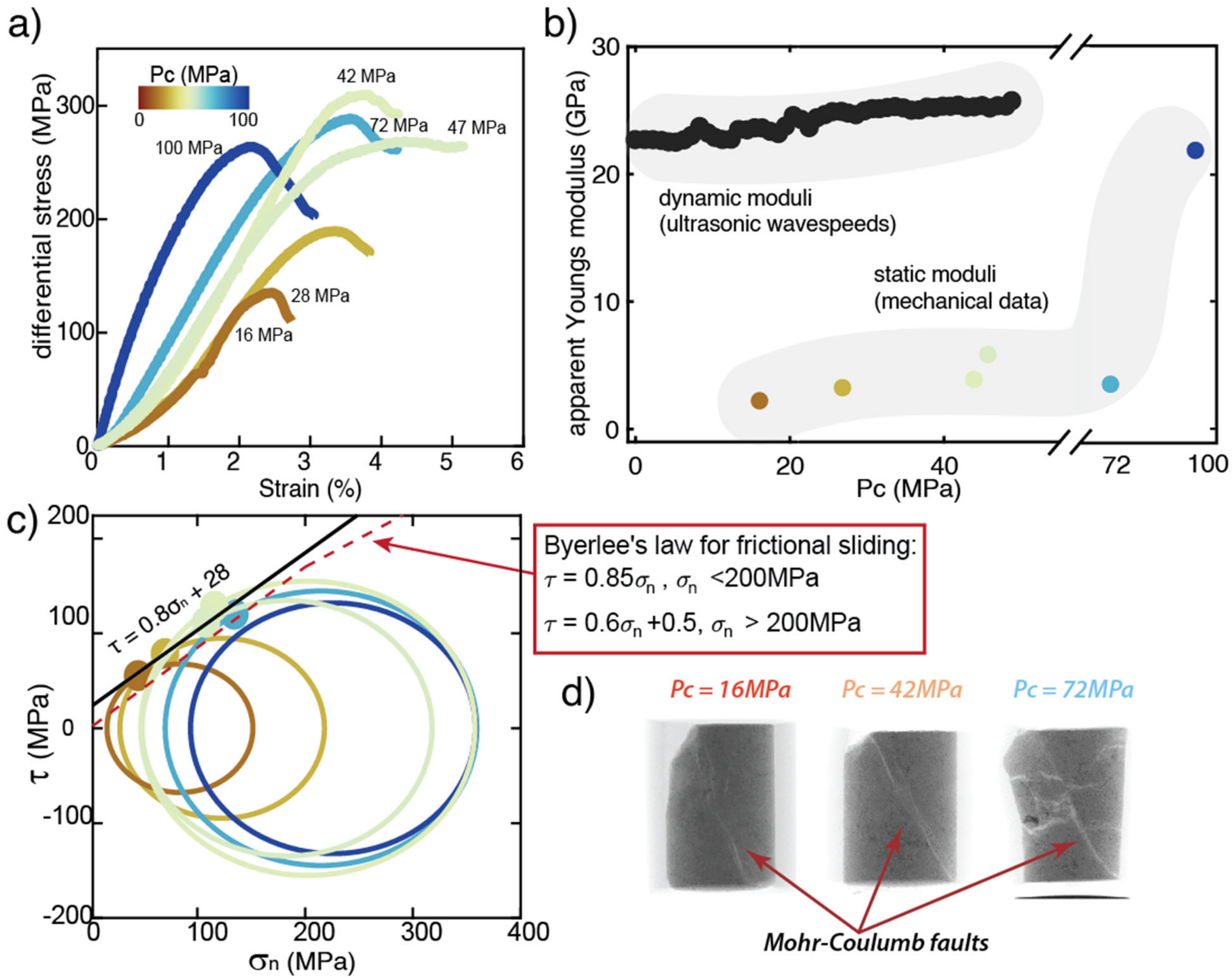

Figure 1: Mechanical results from deformation tests, represented as a) stress/strain curves, colored by confining pressure, b) observed Youngs moduli from ultrasonic and mechanical data, c) Mohr circles, with a tangent line indicating the Mohr-Coulomb failure envelope, large dots represent fault orientation developed at failure and d) CT images of deformed samples, with final faults from peak stress indicated.

3. Results

3.1. Mechanical data

The peak strength of the samples generally increased with confining pressure before reaching a maximum at ~50 MPa Pc (Figure 1a). Above ~50MPa confining pressure, peak strength decreased with increasing confining pressure. The σ_1 did not exceed ~350 MPa in any experiment, and so increases in confining pressure above 50 MPa lead to decreases in differential stress (Figure 1c). In all cases, the strain at peak strength at the point of failure remained close to 3%.

The failure envelopes of the experimentally deformed samples are represented as Mohr circles in Figure 2c. These Mohr circles are a graphical representation of the stress state within a rock at the point of failure, plotted in normal stress (σ_n) vs. shear stress (τ) space such that

$$\sigma_n = \frac{\sigma_1+\sigma_3}{2} + \frac{\sigma_1-\sigma_3}{2}\cos 2\theta \; ; \; \tau = \frac{\sigma_1-\sigma_3}{2}\sin 2\theta \, ,$$

where θ is the orientation of the normal to the fault plane with respect to σ_1. The Mohr-Coulomb failure envelope tangent to the circles indicates the stress conditions expected at failure:

$\tau = 0.8\sigma_n + 28$ (units in MPa).

This linear failure envelope is valid only for samples deformed below ~50 MPa Pc. Byerlee's Law, which defines the shear stress needed to slide rocks along a pre-existing fault surface, falls below the range of stress states recorded during deformation tests, as expected for the deformation of intact rocks. Notably, no test was able to reach σ_1 greater than 350 MPa; the three highest-pressure tests all failed at this point.

During several tests of up to 50 MPa confining pressure, we monitored sound velocities using the piezoelectric sensors placed above and below the sample (See Supplementary Table 1). From these measurements, we characterized dynamic (unrelaxed) Youngs moduli via p- and s-wave arrival times,

$$E_{dyn} = \frac{\rho V_S^2(3V_P^2-4V_S^2)}{V_P^2-V_S^2}.$$

We compared the unrelaxed, microscale E_{dyn} with the observed macroscale Youngs modulus derived from mechanical data on stress, σ, and strain, ε, such that

$$E_{qs} = \frac{\sigma}{\epsilon}\,.$$

As materials are stiffer at higher frequencies and shorter length scales (Jackson, 2015), the calculated Youngs modulus is higher during dynamic probing than during quasistatic bulk deformation (Figure 1b).

3.2. Ultrasonic probes

3.2.1. Acoustic emissions

All samples released energy via microcracking, both during pressurization and deformation. Microcracking occurred at all sampled pressures (Figure 2a, 2d). The integrated power and maximum amplitudes of each AEs decreased slightly with increasing differential stress ($|\sigma_1 - \sigma_3|$) (Figure 2b, 2e), and the power-to-noise ratio was largest for low values of σ_1 (Figure 2c, 2f). Many of these energetically dissipative events occurred during the nominally "elastic" deformation period, when differential stress is low and no energy release is expected. The material also emitted energy through microcracking during isotropic pressurization cycles (Figure 3d), when differential stress is zero.

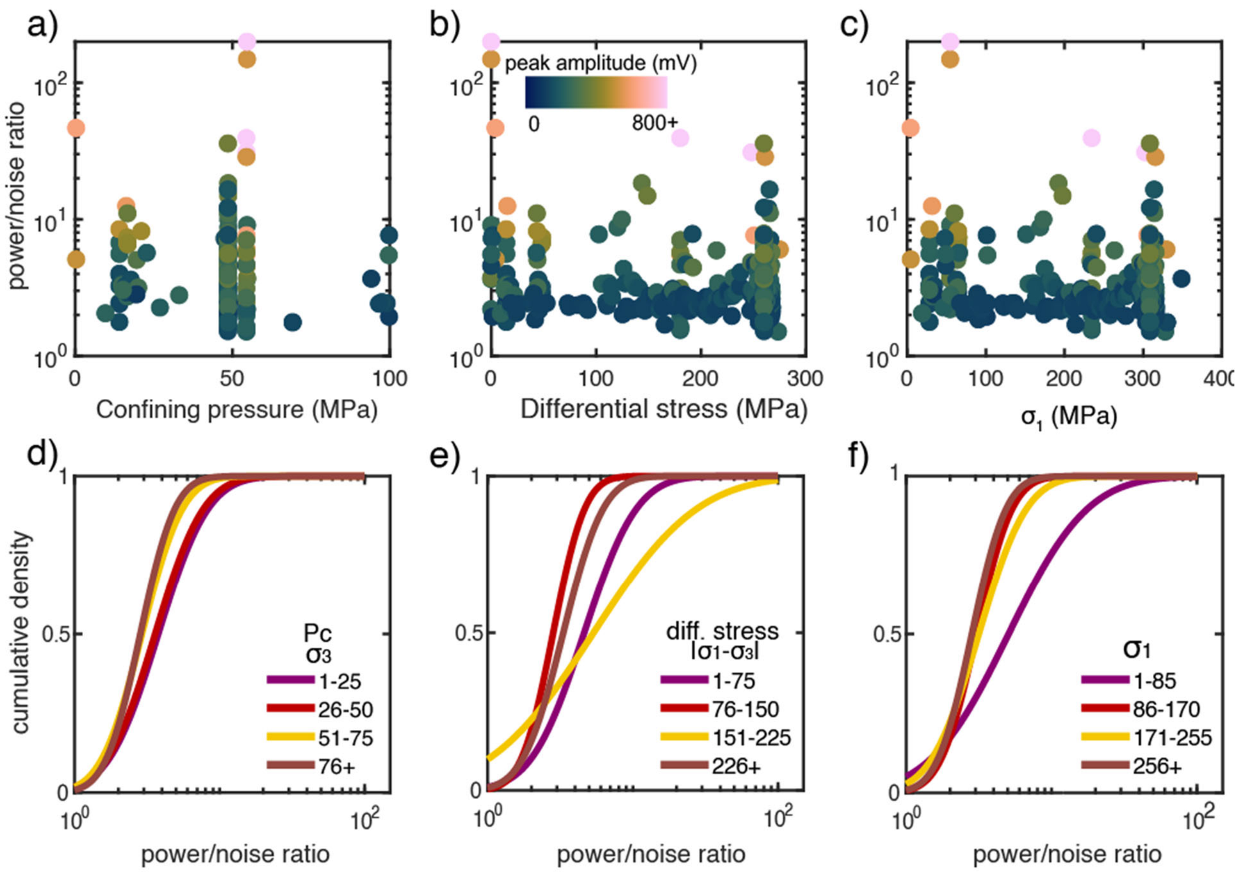

Figure 2: (a-c) Power of AEs, normalized by noise threshold for each test, as a function of a) confining pressure, b) differential stress, c) σ_1. Each point represents one AE event, and is colored by the maximum amplitude of that even following the colorbar in panel b). (d-f) Lognormal cumulative distribution functions of total power per event, evolving as a function of d) confining pressure, e) differential stress, and f) σ_1. Colored lines correspond to specific stress ranges, in MPa, which are defined specifically for each panel in its interior legend.

3.2.2. Ultrasonic pulsing

To determine wavespeeds as a function of pressure, we sent ultrasonic pulses through a sample while cycling confining pressure between 0 and 50 MPa, (Figure 3a, 3b, 3c). This procedure allowed us to examine if pressure oscillations changed the internal structure of our material and validate our results. We examined the entire waveform to see how the structure is affecting throughgoing waves (Figure 3d, 3e). The amplitudes and arrival times of throughgoing waves mimicked the pressure conditions, such that at lower pressures, comparable parts of the waveform arrived later, and at higher pressures, they arrived earlier (Figure 3d). The waveforms also remained similar at the same pressure even after a pressurization-depressurization cycle and associated AEs (Figure 3e; S5), suggesting that the modifications to internal structure of the material occur on smaller length scales than sampled by ultrasonic waves and therefore would not be visible to seismic waves, regardless of the pressure history.

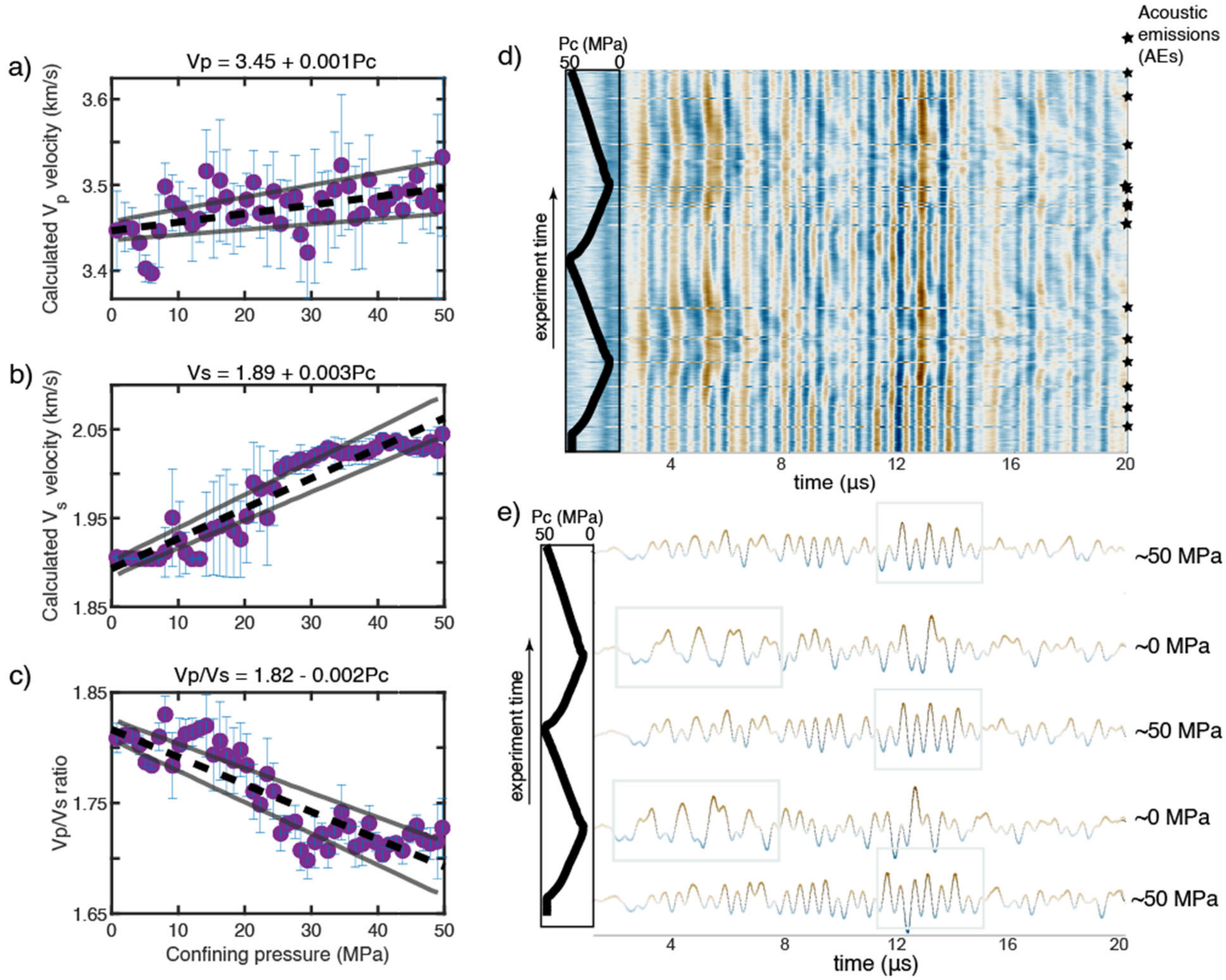

Figure 3: Results from ultrasonic pulsing during confining pressure oscillation. a) Vp wavespeeds. b) Vs wavespeeds. c) Vp/Vs ratio. For a-c, linear trendlines are shown in black, with grey lines denoting 90% confidence interval. d) Two full depressurization-repressurization cycles and resultant waveforms. Black line indicates pressure conditions. Waveforms are stacked with increasing experimental time, and color corresponds with amplitude over wavelength time, from blue (high negative amplitude) to brown (high positive amplitude). Horizontal, discontinuous lines marked with stars are energetic acoustic emission events, which are separate from the pulsed ultrasonic waves shown here. e) Sample waveforms from 0 and 50 MPa confining pressure at each inflection point in the cycle. Similar parts of the waveform at 0 and 50 MPa are highlighted in light grey boxes. See Supplementary Information for further discussion of waveform analysis (S4-6).

4. Discussion

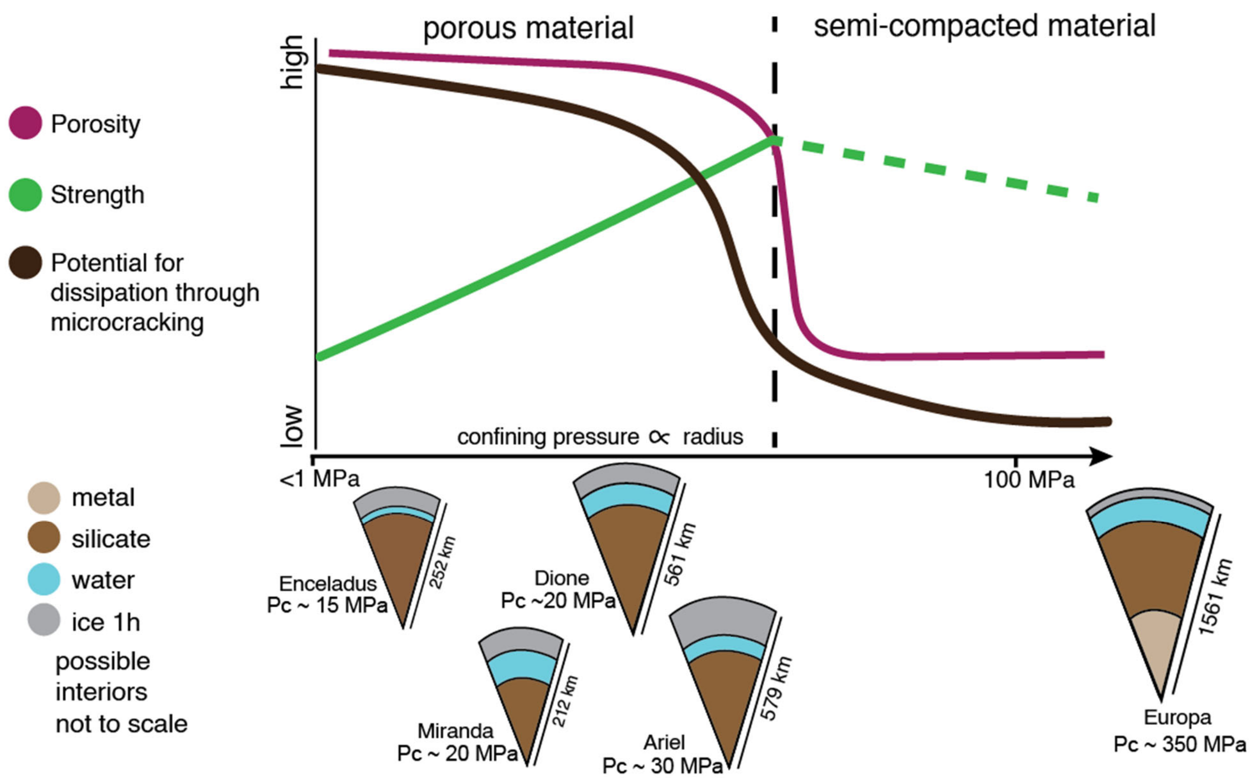

Figure 4: A conceptual diagram showing the effects of confining pressure on porosity, strength, and the power released via microcracking. Sample interior models for small icy moons are shown in order of increasing Pc at the ocean-rock interface, based on estimates from PlanetProfile by Vance et al (2018).

The above results show that the mechanical and acoustic properties of chondritic material, and therefore the cores of icy moons, are dependent on confining pressure. Several of these relationships are depicted schematically in Figure 4.

4.1. Discussion of mechanical data

Chondritic material initially strengthens with increasing confining pressure, then undergoes a drop in peak differential stress above confining pressures >50 MPa (Figure 1a, 1c). This behavior is similar to the "cap model" for compaction and deformation of porous Earth materials. In the cap model porosity drops steadily with increasing pressure before dropping rapidly at a point of compactive yield (C*), where the load-bearing framework collapses and above which cataclastic flow takes over as the primary mode of deformation (Wong and Baud, 2012).

Pore closure may therefore proceed in a predictable, yet discontinuous manner across icy moon environments. The maximum pressure at which porosity is maintained within a rocky interior should decrease with increasing Pc, then suddenly drop, rather than a slow closure similar to that within the outer layers of rocky planets as is often assumed in planetary models (e.g. Vance et al., 2018). The pores do not close entirely at this point, but most porosity is lost. It is possible that the maximum normal stress seen in our test, 350 MPa, represents the condition for total pore closure. Assumptions of density and permeability within cores should see a similar jump. These observations indicate that the mechanisms of deformation may be different in larger moons than in smaller moons, due to the increased confining pressures from increased overburden at the rock-ocean or rock-ice interface. In bodies where rocky interiors are under higher confining pressures, pore closure effects may not be as important and material may be stiffer; in lower-pressure environments, material may deform more easily.

Viscoelastic deformation of silicate interiors has been suggested as a mechanism for heat generation and tidal dissipation in Enceladus and Europa (Kang et al., 2020; Liao et al., 2020; Rovira-Navarro et al., 2022), but a true viscous response is unlikely in a cold, chondritic layer. Silicates typically require elevated pressures and temperatures for viscous deformation (e.g. Kohlstedt and Hansen, 2015). Brittle creep, a mechanism that is active in silicate rocks at low pressures and temperatures (Bernabé and Peč, 2022; Brantut et al., 2013) may generate an additional apparent viscous response, contributing to the total heat dissipation via microcracking. Similar effects may arise from pore closure and reopening. While not truly a viscous response, the presence of brittle creep could serve as a nonlinear viscous element over short timescales and thus should be considered in models for viscoelastic core deformation.

4.2. Discussion of acoustic and ultrasonic data

Dissipative acoustic emissions from microcracking events occurred at all pressures sampled, even at low differential stresses, indicating that even small changes to local stresses can initiate cracks (Figure 2). The Vp/Vs ratio also decreased with increasing confining pressure (Figure 3c), which occurs as damage increases (Wang et al., 2012). We suggest that microcracking could be continuously occurring in rocky interiors of icy satellites, where deviatoric stresses can be on the order of 1 MPa or higher, changing periodically with the orbit of the satellite (Gao and Stevenson, 2013; McKinnon, 2013). As these cracks occurred during the nominally elastic component of deformation (low differential stress, low strain; see Figure 2b, 2e), we suggest that that the energy from these microscale plastic mechanisms should be associated with the apparent viscous response necessary for dissipation in the silicate core.

Moons with thinner crusts and oceans could receive proportionally more heat over their lifetimes from the deformation of their rocky interiors than larger moons, as their cores will be more deformable at low pressures and therefore able to dissipate heat during viscoelastic deformation. Local values of σ_1 will be lower in smaller moons as well, corresponding to the most energetic cracking events seen in our tests (Figure 2c, 2f). As this energy is released, it could contribute to processes such as ice overturn, ocean maintenance, and possibly even geyser activity as seen on Enceladus' south pole. Pore fluids change the local stress state by lowering the effective pressure, so that materials at the ocean-silicate interface could experience even more fracture than we observe in lab. Additionally, while our deformation experiments are conducted at relatively slow strain rates, they are not identical to timescales and frequencies of tidal deformation. Under realistic tidal forcing periods, the strength of porous rocks is lower (Bagde and Petroš, 2009; Peng et al., 2020), increasing the likelihood of cracking in response to small stress changes. One excellent opportunity for future laboratory studies is the measurement of acoustic properties of aqueously altered chondritic material, which should exist at the rock-ocean boundary.

In addition to releasing heat at the time of their formation, cracks create new surface area. Modeling by Rovira-Navarro et al. (2022) found that rock-water interaction (via increasing permeability) increases dissipation throughout a porous core. Fresh surface area would encourage serpentinization, which has been suggested as a mechanism for generating hydrogen within the oceans of icy bodies (Kamata et al., 2019; McCollom et al., 2022; Neveu et al., 2015; Vance and Melwani Daswani, 2020) or cultivation of organic materials which have risen to Titan's surface (Castillo-Rogez and Lunine, 2010). Many of these reactions include volume increase which modifies the local stress field, encouraging further cracking within the silicate body and providing a self-sustaining heating process.

5. Conclusions

We characterized the mechanical properties of stony chondritic material under a range of confining pressures, defined a failure envelope, measured wavespeeds, and retrieved both static and dynamic elastic moduli. The mechanical results suggest that porosity decreases significantly at lab confining pressure of ~50 MPa, such that the silicate interiors of larger icy moons will be relatively dense and impermeable. The interiors of larger moons are less deformable, and therefore contribute proportionally less energy in response to tidal forcing, than those of smaller moons. We also observed semi-continuous energy release arising from microcracking under small changes to stress. These microcracks may represent an apparent viscous response which enhances heat dissipation within rocky cores and mantles. The energy release from microcracking occurred during pressurization and depressurization as well, and transmissivity of the material (likely dependent on its porosity) was a function of current confining pressure rather than pressure history. Pressure, and the resultant amount of porosity that a material can maintain, is therefore a strong control on the dissipative potential of silicate interiors. These findings are useful for determining the level of heat generated in the cores and mantles of icy moons, which may then drive ocean circulation and/or maintenance. We also see that the release of energy persists as deformation continues, indicating that ongoing deformation on a diurnal timescale may remain important for the total heat flux of an icy body.

Acknowledgements: CS received support from Massachusetts Space Grant fellowship and MathWorks. Figures were plotted using perceptually uniform colormaps from Crameri (2021). CORD laboratory technician support by NSF grant # 2054414 is gratefully acknowledged. Thank you to Veronique LeRoux for CT scans, Mark Panning, Mohit Melwani Deswani, and Laurent Pou for discussions on icy moon interiors, and to Rick Binzel for early input on the project.

Data Availability Statement: All mechanical, ultrasonic, and acoustic data can be found at https://zenodo.org/records/10211457 (Seltzer, 2023).

Aygün, B., Čadek, O., 2022. A new approach to modeling the tidal dissipation in subsurface oceans of icy moons of Jupiter and Saturn (other). oral. https://doi.org/10.5194/epsc2022-968

Bagde, M.N., Petroš, V., 2009. Fatigue and dynamic energy behaviour of rock subjected to cyclical loading. International Journal of Rock Mechanics and Mining Sciences 46, 200–209. https://doi.org/10.1016/j.ijrmms.2008.05.002

Bernabé, Y., Peč, M., 2022. Brittle Creep and Failure: A Reformulation of the Wing Crack Model. Journal of Geophysical Research: Solid Earth 127, e2022JB024610. https://doi.org/10.1029/2022JB024610
Brantut, N., Heap, M.J., Meredith, P.G., Baud, P., 2013. Time-dependent cracking and brittle creep in crustal rocks: A review. Journal of Structural Geology 52, 17–43. https://doi.org/10.1016/j.jsg.2013.03.007
Castillo-Rogez, J.C., Lunine, J.I., 2010. Evolution of Titan's rocky core constrained by Cassini observations. Geophysical Research Letters 37. https://doi.org/10.1029/2010GL044398
Crameri, F., 2021. Scientific colour maps. https://doi.org/10.5281/zenodo.5501399
Eitzen, D.G., Wadley, H.N.G., 1984. Acoustic Emission: Establishing the Fundamentals. J. RES. NATL. BUR. STAN. 89, 75. https://doi.org/10.6028/jres.089.008
Flynn, G.J., Consolmagno, G.J., Brown, P., Macke, R.J., 2018. Physical properties of the stone meteorites: Implications for the properties of their parent bodies. Geochemistry 78, 269–298. https://doi.org/10.1016/j.chemer.2017.04.002
Gao, P., Stevenson, D.J., 2013. Nonhydrostatic effects and the determination of icy satellites' moment of inertia. Icarus 226, 1185–1191. https://doi.org/10.1016/j.icarus.2013.07.034
Ghaffari, H.O., Mok, U., Pec, M., 2021. On calibration of piezoelectric sensors with laser doppler vibrometer. The Journal of the Acoustical Society of America 150, 2503–2513. https://doi.org/10.1121/10.0006445
Ghaffari, H.O., Nasseri, M.H.B., Young, R.P., 2014. Faulting of Rocks in a Three-Dimensional Stress Field by Micro-Anticracks. Sci Rep 4, 5011. https://doi.org/10.1038/srep05011
Hogan, J.D., Kimberley, J., Hazeli, K., Plescia, J., Ramesh, K.T., 2015. Dynamic behavior of an ordinary chondrite: The effects of microstructure on strength, failure and fragmentation. Icarus 260, 308–319. https://doi.org/10.1016/j.icarus.2015.07.027
Jackson, I., 2015. Properties of Rocks and Minerals: Physical Origins of Anelasticity and Attenuation in Rock, in: Treatise on Geophysics. Elsevier, pp. 539–571. https://doi.org/10.1016/B978-0-444-53802-4.00045-2
Kamata, S., Nimmo, F., Sekine, Y., Kuramoto, K., Noguchi, N., Kimura, J., Tani, A., 2019. Pluto's ocean is capped and insulated by gas hydrates. Nat. Geosci. 12, 407–410. https://doi.org/10.1038/s41561-019-0369-8
Kang, W., Bire, S., Campin, J.-M., Sotin, C., German, C., Thurnherr, A., Marshall, J., 2020. Differing Enceladean ocean circulation and ice shell geometries driven by tidal heating in the ice versus the core.
Kimberley, J., Ramesh, K.T., 2011. The dynamic strength of an ordinary chondrite. Meteoritics & Planetary Science 46, 1653–1669. https://doi.org/10.1111/j.1945-5100.2011.01254.x
Kohlstedt, D.L., Hansen, L.N., 2015. Constitutive Equations, Rheological Behavior, and Viscosity of Rocks, in: Treatise on Geophysics. Elsevier, pp. 441–472. https://doi.org/10.1016/B978-0-444-53802-4.00042-7
Kuskov, O.L., Kronrod, V.A., 2005. Internal structure of Europa and Callisto. Icarus, Europa Icy Shell 177, 550–569. https://doi.org/10.1016/j.icarus.2005.04.014
Lei, X., Ma, S., 2014. Laboratory acoustic emission study for earthquake generation process. Earthq Sci 27, 627–646. https://doi.org/10.1007/s11589-014-0103-y
Li, X., Si, G., Oh, J., Canbulat, I., Xiang, Z., Zhang, X., 2021. Laboratory characterisation of anisotropic and heterogeneous damage of rock sample using acoustic emission and ultrasonic monitoring technologies. IOP Conf. Ser.: Earth Environ. Sci. 861, 022040. https://doi.org/10.1088/1755-1315/861/2/022040
Liao, Y., Nimmo, F., Neufeld, J.A., 2020. Heat Production and Tidally Driven Fluid Flow in the Permeable Core of Enceladus. Journal of Geophysical Research: Planets 125, e2019JE006209. https://doi.org/10.1029/2019JE006209

Mair, K., Elphick, S., Main, I., 2002. Influence of confining pressure on the mechanical and structural evolution of laboratory deformation bands. Geophysical Research Letters 29, 49-1-49–4. https://doi.org/10.1029/2001GL013964

McCollom, T.M., Klein, F., Ramba, M., 2022. Hydrogen generation from serpentinization of iron-rich olivine on Mars, icy moons, and other planetary bodies. Icarus 372, 114754. https://doi.org/10.1016/j.icarus.2021.114754

McKinnon, W.B., 2013. The shape of Enceladus as explained by an irregular core: Implications for gravity, libration, and survival of its subsurface ocean. Journal of Geophysical Research: Planets 118, 1775–1788. https://doi.org/10.1002/jgre.20122

Mulliken, A.D., Boyce, M.C., 2006. Mechanics of the rate-dependent elastic–plastic deformation of glassy polymers from low to high strain rates. International Journal of Solids and Structures 43, 1331–1356. https://doi.org/10.1016/j.ijsolstr.2005.04.016

Néri, A., Guyot, F., Reynard, B., Sotin, C., 2020. A carbonaceous chondrite and cometary origin for icy moons of Jupiter and Saturn. Earth and Planetary Science Letters 530, 115920. https://doi.org/10.1016/j.epsl.2019.115920

Neumann, W., Kruse, A., 2019. Differentiation of Enceladus and Retention of a Porous Core. ApJ 882, 47. https://doi.org/10.3847/1538-4357/ab2fcf

Neveu, M., Desch, S.J., Castillo-Rogez, J.C., 2015. Core cracking and hydrothermal circulation can profoundly affect Ceres' geophysical evolution. Journal of Geophysical Research: Planets 120, 123–154. https://doi.org/10.1002/2014JE004714

Nimmo, F., Pappalardo, R.T., 2016. Ocean worlds in the outer solar system. Journal of Geophysical Research: Planets 121, 1378–1399. https://doi.org/10.1002/2016JE005081

O'Ghaffari, H., Peč, M., Mittal, T., Mok, U., Chang, H., Evans, B., 2023. Microscopic defect dynamics during a brittle-to-ductile transition. Proceedings of the National Academy of Sciences 120, e2305667120. https://doi.org/10.1073/pnas.2305667120

Paterson, M.S., 1990. Rock Deformation Experimentation, in: The Brittle-Ductile Transition in Rocks. American Geophysical Union (AGU), pp. 187–194. https://doi.org/10.1029/GM056p0187

Peng, K., Zhou, J., Zou, Q., Song, X., 2020. Effect of loading frequency on the deformation behaviours of sandstones subjected to cyclic loads and its underlying mechanism. International Journal of Fatigue 131, 105349. https://doi.org/10.1016/j.ijfatigue.2019.105349

Pohl, L., Britt, D.T., 2020. Strengths of meteorites—An overview and analysis of available data. Meteoritics & Planetary Science 55, 962–987. https://doi.org/10.1111/maps.13449

Ramesh, K.T., Stickle, A.M., Kimberley, J., 2017. Rocks, Shocks and Asteroids, and Some Interesting Research Directions in Mechanics: 2015 Murray Lecture Paper. Experimental Mechanics 57, 1149–1159. https://doi.org/10.1007/s11340-017-0324-9

Rovira-Navarro, M., Katz, R.F., Liao, Y., van der Wal, W., Nimmo, F., 2022. The Tides of Enceladus' Porous Core. Journal of Geophysical Research: Planets 127, e2021JE007117. https://doi.org/10.1029/2021JE007117

Seltzer, C., 2023. Supporting data for "Mechanical properties of the rocky interiors of icy moons" [DATASET]. https://doi.org/10.5281/zenodo.10211457

Styczinski, M.J., Vance, S.D., Melwani Daswani, M., 2022. PlanetProfile: Self-consistent interior structure modeling for terrestrial bodies in Python (preprint). Planetology. https://doi.org/10.1002/essoar.10512890.1

Tobie, G., Mocquet, A., Sotin, C., 2005. Tidal dissipation within large icy satellites: Applications to Europa and Titan. Icarus, Europa Icy Shell 177, 534–549. https://doi.org/10.1016/j.icarus.2005.04.006

Vance, S.D., Melwani Daswani, M., 2020. Serpentinite and the search for life beyond Earth. Philosophical Transactions of the Royal Society A: Mathematical, Physical and Engineering Sciences 378, 20180421. https://doi.org/10.1098/rsta.2018.0421

Vance, S.D., Panning, M.P., Stähler, S., Cammarano, F., Bills, B.G., Tobie, G., Kamata, S., Kedar, S., Sotin, C., Pike, W.T., Lorenz, R., Huang, H.-H., Jackson, J.M., Banerdt, B., 2018. Geophysical

Investigations of Habitability in Ice-Covered Ocean Worlds. Journal of Geophysical Research: Planets 123, 180–205. https://doi.org/10.1002/2017JE005341

Voropaev, S.A., Kocherov, A.V., Lorenz, C.A., Korochantsev, A.V., Dushenko, N.V., Kuzina, D.M., Nugmanov, I.I., Jianguo, Y., 2017. Features in constructing a certificate of strength of extraterrestrial material by the example of the Chelyabinsk meteorite. Dokl. Phys. 62, 486–489. https://doi.org/10.1134/S1028335817100111

Voropaev, S.A., Nugmanov, I.I., Dushenko, N.V., Jianguo, Y., 2020. Dependence of the Elastic Properties of H5-Chondrites (NWA 12370) on Pressure. Dokl. Phys. 65, 383–386. https://doi.org/10.1134/S1028335820110105

Wang, X.-Q., Schubnel, A., Fortin, J., David, E.C., Guéguen, Y., Ge, H.-K., 2012. High Vp/Vs ratio: Saturated cracks or anisotropy effects? Geophysical Research Letters 39. https://doi.org/10.1029/2012GL051742

Supplementary Information:

Mechanical properties of the rocky interiors of icy moons

C. Seltzer, H.O. Ghaffari, M. Peč

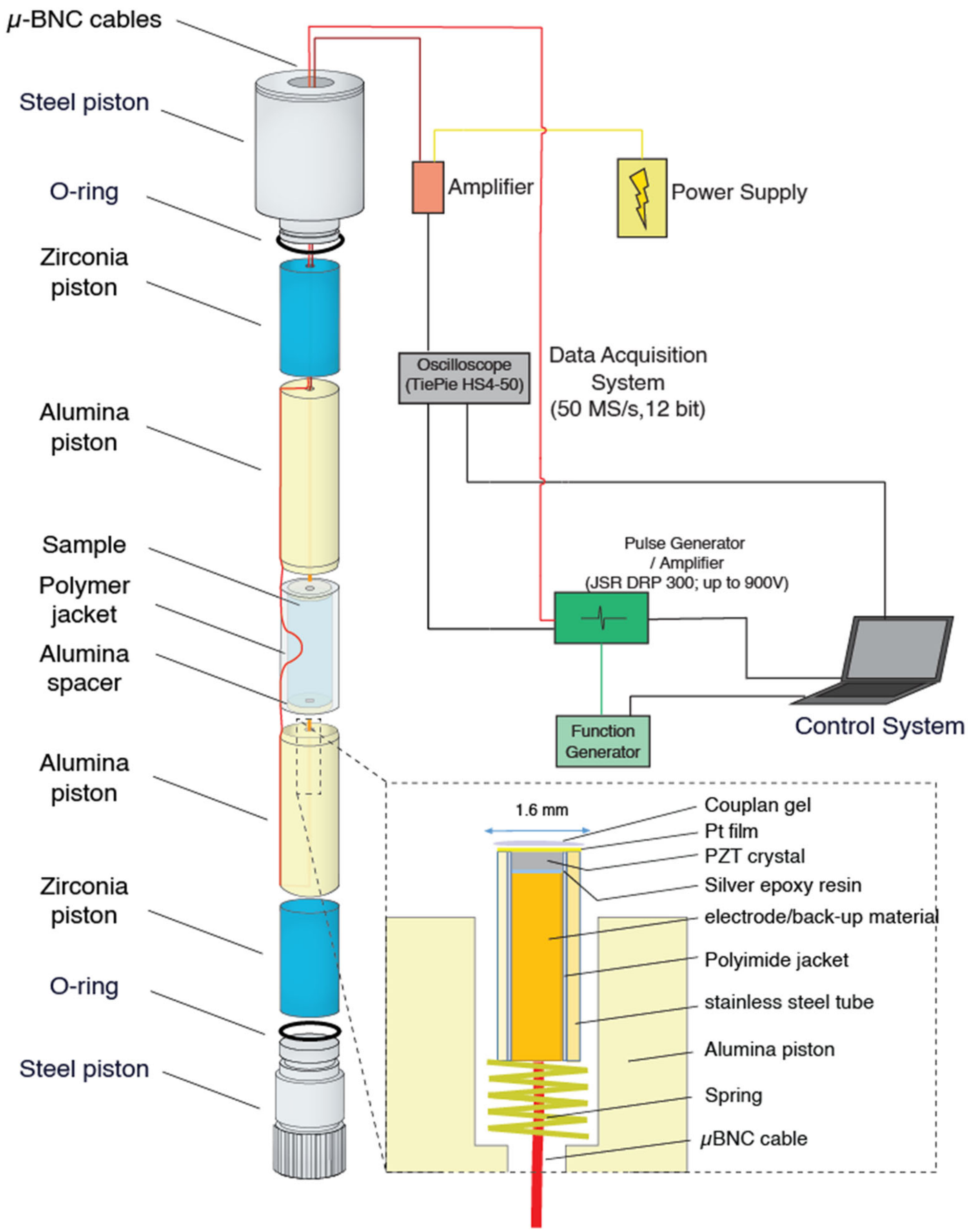

Figure S1: Schematic of our sample setup and ultrasonic instrumentation method.

All experiments were conducted in a Paterson gas medium deformation apparatus, PI-5, in the Rock Deformation Laboratory at MIT. Two custom-made miniature piezo-sensors with stainless steel jacket were threaded through the central hole in the pistons, most commonly used for thermocouples, and mechanically coupled with meteorite sample using springs, as shown in inset. The response of sensors was evaluated before, during and after the tests (using pulse-echo method) to verify the sensors were not lost or weakened by spring-loading process. Signals passed through μ-BMC wires, an amplifier set to amplify signals at 60 dB, and were recorded in a TiePie HS4-50 oscilloscope.

Table T1: experimental parameters for each test.

	Max Pc (MPa)	initial length (mm)	diameter (mm)	max diff. stress (MPa)	dx rate (mm/min)	strain rate (s^{-1})	T (K)	AEs
001_CS_PI	54	11.73	6.75	428	0.072	1E-05	295	yes
009_CS_PI	28	10.05	6.77	193	0.029	5E-05	295	no
010_CS_PI	16	10.55	6.76	138	0.032	5E-05	295	no
012_CS_PI	72	11.5	6.75	289	0.035	5E-05	295	yes
013_CS_PI	42	9.34	6.75	214	0.028	5E-05	295	yes
015_CS_PI	100	8.93	6.74	265	0.027	5E-05	295	yes
017_CS_PI	20	7.82	6.66	50	0.023	5E-05	295	yes
019_CS_PI	40	6.72	6.72	72	0.023	5E-05	295	no
032_CS_PI	45	7.3	6.25	265	0.022	5E-05	295	yes
033_CS_PI	50	7.3	6.75	311	0.022	5E-05	295	yes
037_CS_PI	47	7.29	6.66	268	0.022	5E-05	295	yes

Table T1. Each test is recorded by name in the farthest left column. Pc = confining pressure, dx rate = displacement rate, T = temperature. AEs column indicates whether sensors were in place and able to record acoustic emissions.

On the calibration of amplifiers and piezoelectric sensors:

The response of amplifiers at 60 dB was tested at room conditions by sending a sinusoidal pulse with different frequencies and amplitudes through the same length of BNC cables used in the real set-up of our tests. The response of the amplifier is flat amplification of ~57 dB up to 1.5 MHz, after which there was an exponential decreasing of amplification from 57 dB to 35 dB at frequencies up to ~15 MHz. The majority of recorded signals were in the frequency range ~50 kHz to 2 MHz. Note that the employed amplifiers did not distort or change the shape of the sine waves for excited signals below 500 mV, and correctly transferred the frequency of the input waves.

To calibrate the response of the sensor, we used a 3D laser Doppler vibrometer (LDV) which can measure the vibration rates in three perpendicular directions (Ghaffari et al., 2021) and is sensitive to signals from 5kHz to ~300kHz. We calibrated these sensors within a frequency range <400kHz, in order to set a lower limit in measuring velocities and displacements. The sensor (instrument) response can be isolated once we identify the amplitude-power of a reference sensor or probe ($P_{LDV}(\omega)$) and of a test sensor ($P_{PZT}(\omega)$) for the same vibration. Here, the source could be a fixed source generated by a vibrating sensor due to sinusoidal waveforms, or an impulse-electrical signals generating a train of waves with different frequencies in the source sensor. The instrument response or transform function in power-frequency domain is defined such that $I(\omega) = \frac{P_{PZT}(\omega)}{P_{LDV}(\omega)}$. For an ideal sensor, $I(\omega)$=1. However, here we have partial overlap of frequencies between the two sensors, so our instrument response function is valid for the domain from 40kHz-300kHz.

We calibrated the needle (miniature) sensors used in our experiments in two different set-ups:
I) in the first set-up, a pulsing sensor was triggered with a sweep mode of sinusoidal wave pulses at frequencies of 10 kHz to 5 MHz. The receiver sensor receives the signal directly. A thin film of mica is used to prevent electrical noise and interference. The pulsing transducer's pressure field (radiation field) is characterized independently with pulse-echo (in air) method, where the sensor receives a short ~100 ns electrical pulse and the vibration of the sensor is recorded at 0 dB amplification. The energy input of electrical pulse is set to be equal with amplitude of pulses in the main set-up. We use spectral analysis to obtain amplitudes for each frequency domain (at bin size of 10 kHz), then integrated to define total power at each frequency, P(ω). We evaluated the receiver sensor as the main sensing element by its sensitivity (loop gain, insertion loss) parameter, S(dB) = 20 log (V_x/ V_0), where V_x is the amplitude of the received signal in volts at a given frequency and V_0 is the amplitude of transducer excitation in volts at the same frequency. In Figure S2 we show the S-parameter. An almost flat response relative to the source sensor is achieved in the frequency range of 0.35-1.5MHz

II) We also calibrated our sensors with an on-table test (**Figure S2**) in which we used a cylindrical rock sample and two sensors spring-loaded to end surfaces of the sample. One sensor served as a source, pulsing signals through the sample which were received at the other end, where laser beams of LDV measured the velocity components. To compare the response of the receiver sensor with the laser measurements, we calculated an overlapped (80%) 2,048-point fast Fourier transform to calculate the power of the signal. Next, we calculated the average of the power of the waveform over a frequency range from 50 kHz to 300kHz($\langle P\rangle_\omega$) (**Figure S2e**). $\langle P(t)\rangle_\omega$ has a peak-like form and includes a fast-rising phase which is followed by a fast drop (**Figure S2c**). Response of the sensor encoded in $\langle P\rangle_\omega$ closely matches with the z-component of slip velocity profile measured by laser beams. Similarity of out of plane velocity profile to $\langle P(t)\rangle_\omega$ (Figure 3e) yields a lower bound estimate of displacement:

Considering an approximation for particle velocity: $|v(t)| \equiv < P(t) >_\omega$, we find a total integrated displacement $d(t) \equiv \int < P(t) >_\omega dt$ (**Figure S2f**). For the illustrated case in **Figure S2**, the maximum displacement in the sensor location during ~30 μs rise-time of the slip rate is ~1.5 nm. In **Figure S3**, we show this analysis applied to a sample waveform recorded during deformation.

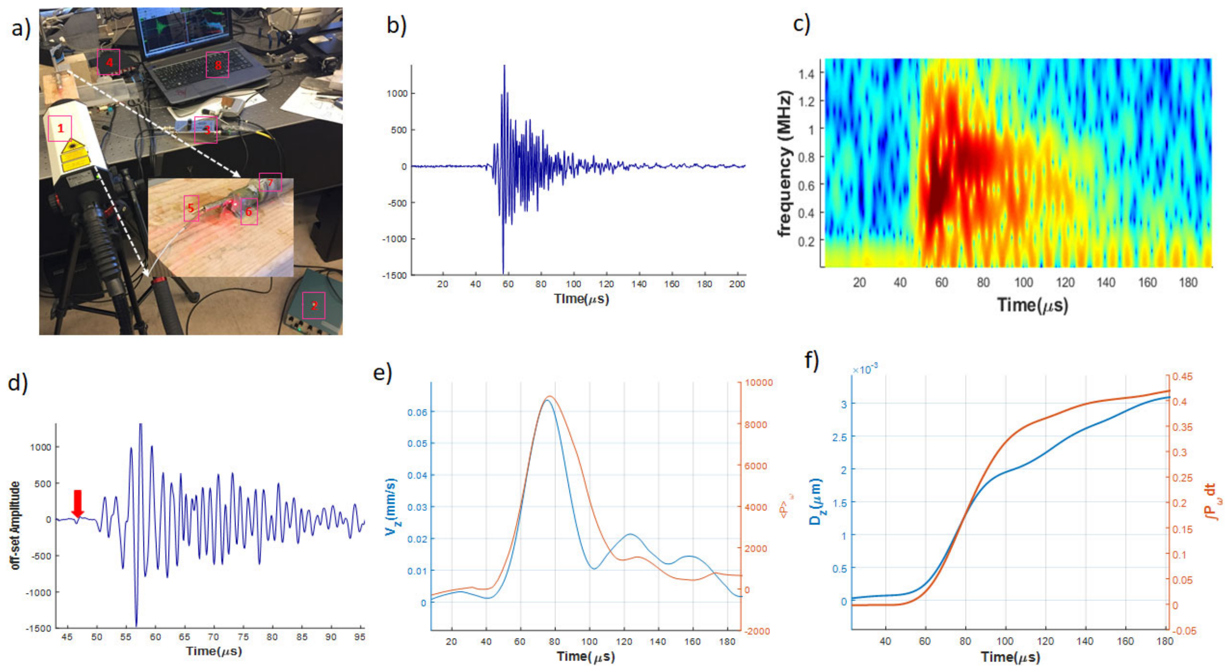

Figure S2. Calibration of the sensors at room conditions with a 3-D laser Doppler vibrometer for signals in the range of $1\ \text{kHz} < \omega < 300\ \text{kHz}$. We used a needle piezo-sensor in contact with a rock sample as the receiver and another sensor as the source. The laser beam is placed in vicinity of the receiver sensor that is amplified at 60 dB, and records vibration rates of the rock sample surface in three perpendicular directions. The out of plane component (z- or dilatational component) is obtained and compared with mean of the magnitudes of FT terms over a certain frequency domain $\langle P\rangle_{\omega}$.

a) Tabletop setup for laser calibration.
b) Full waveform response to laser pulse
c) Frequency-power spectrum for waveform response
d) Truncated waveform, with red arrow indicating arrival time
e) response of the sensor represented with mean power of the signal on the interest frequency domain $\langle P\rangle_{\omega}$, plotted alongside the slip velocity for displacement recorded within the waveform.
f) total displacement and total power during waveform

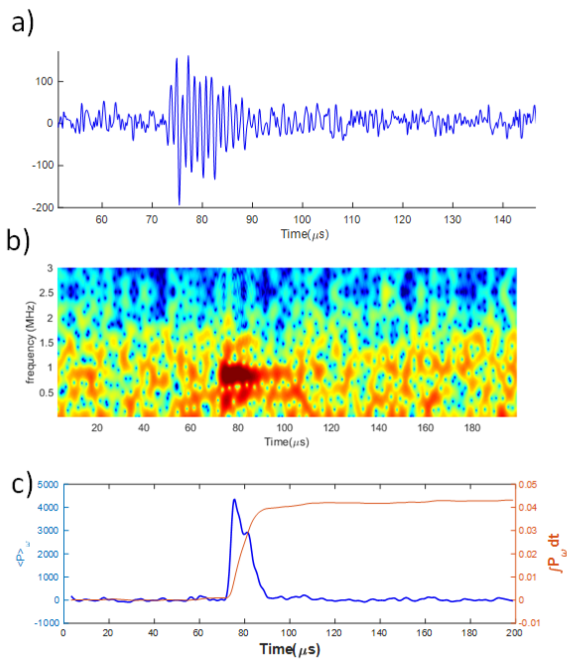

Figure S3. Spectral analysis of a waveform emitted during deformation under confining pressure of 100 MPa. a) Acoustic waveform, b) frequency-power spectrum, c) total power released.

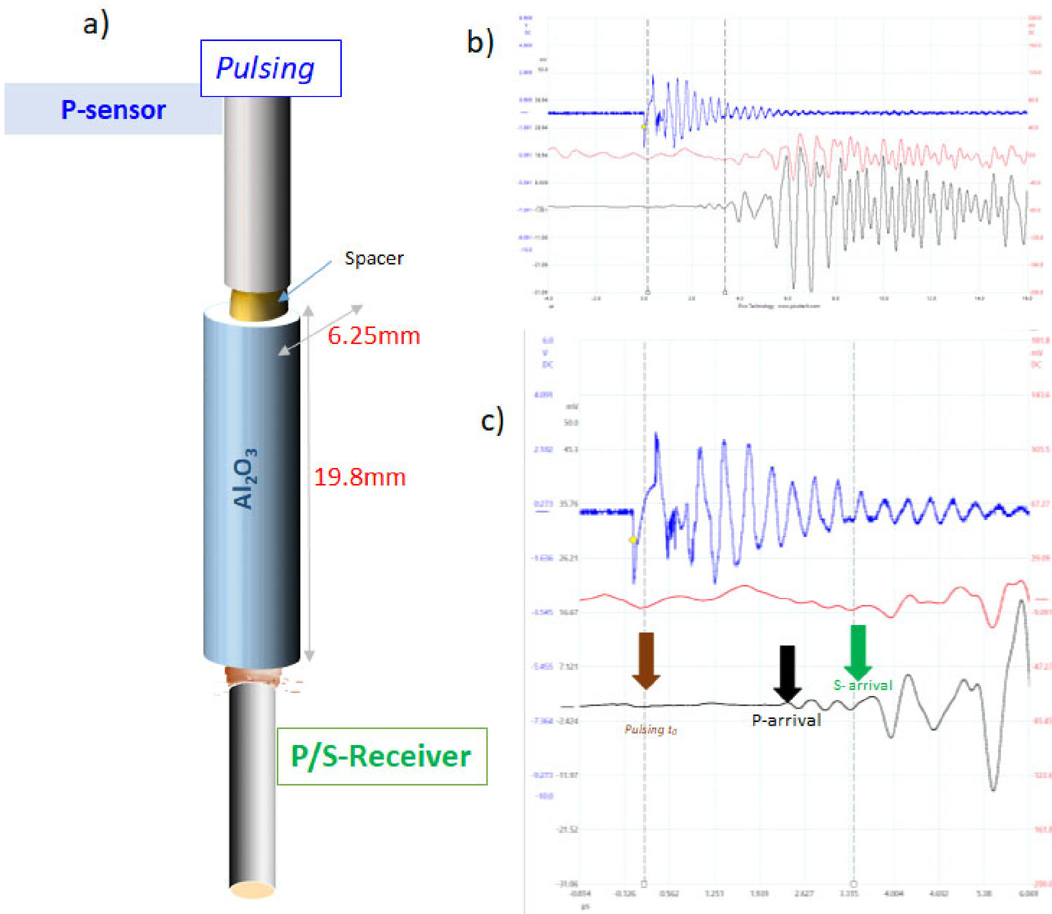

Figure S4: Pulsing-receiving sensor setup and calibration.

a) We used a rod of alumina to calibrate waveforms before picking from real tests. b) Sample waveform from calibration. Alumina sound velocities under room conditions for P and S waves are 9.9 and 6.5 km/s, respectively. c) Wave picking from calibration. There is a weak P arrival, but strong S arrival.

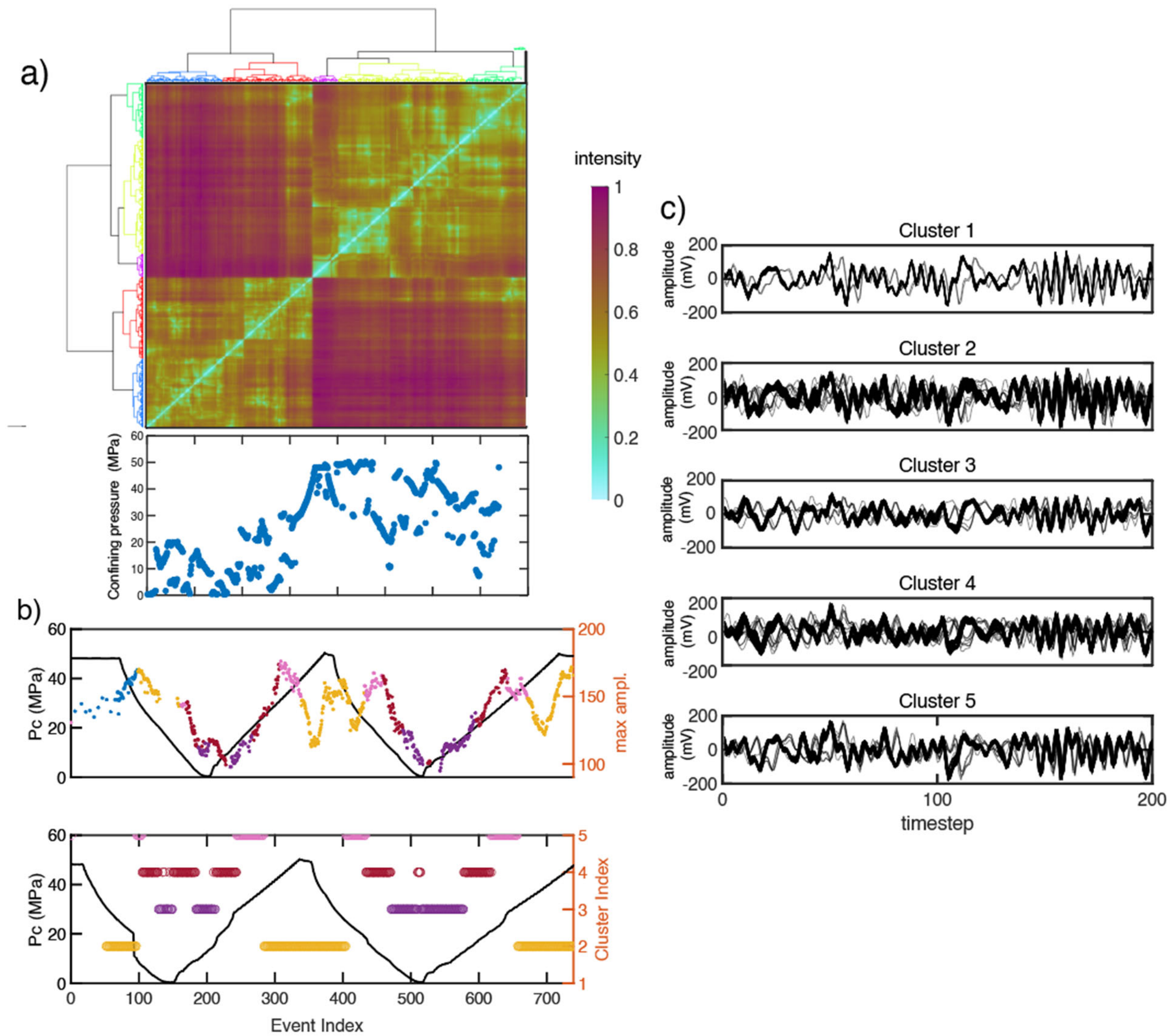

Figure S5: Clustering of active ultrasonic pulses during two cycles of pressurization-depressurization up to 50 MPa Pc. We used a dynamic time warping (DTW) metric to compare 'distance' of waves and used hierarchical clustering. a) Clustergram, accompanied with confining pressure graph, b) Plot of max amplitude and cluster index overlying confining pressure graph, c) waveforms from each cluster.

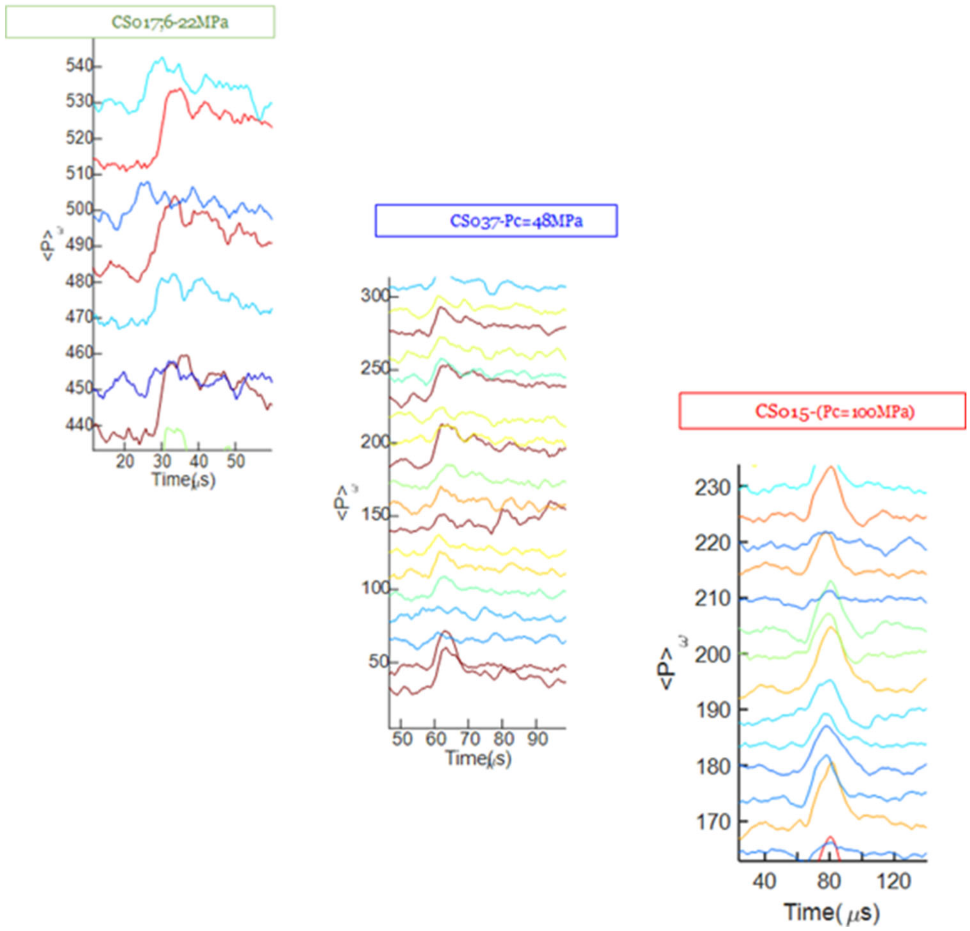

Figure S6: <P(t)> parameter for AEs at three different confining pressures. <P(t)> scales with particle velocity at the sensor location. As pressure increases the signal's skewness change and approaches ~symmetric pulse.